

An Investigation into the Energetics of the Surf Zone
and the Interactions between Turbulence and Bubbles


by

Roblyn Kendall
B.Sc., University of Toronto, 1998

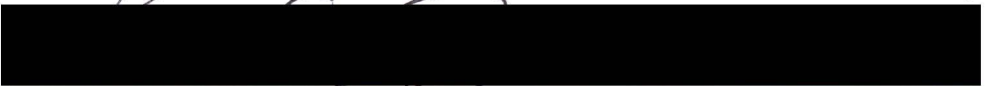
A Thesis Submitted in Partial Fulfillment of the Requirements
for the Degree of
MASTER OF SCIENCE
in the Department of Physics and Astronomy

 We accept this thesis as conforming to the required standard


Dr. D. M. Farmer, Supervisor (Institute of Ocean Sciences)


Dr. C. J. R. Garrett, Departmental Member (Department of
Physics and Astronomy)


Dr. R. Lueck, Outside Member (School of Earth and Ocean Sciences)


Dr. G. B. Deane, External Examiner (Scripps Institution
of Oceanography, La Jolla, California)

© Roblyn Kendall, 2001
University of Victoria

*All rights reserved. This thesis may not be reproduced in whole or in part,
by photocopy or other means, without the permission of the author.*

Supervisor: Dr. David M. Farmer

Abstract

Bubbles and turbulence are produced by breaking waves in the surf zone. Measurements obtained during a field experiment at the beach near Scripps Pier in 1997 found dissipation rates measured beneath the wave troughs to be an order of magnitude less than the divergence of the wave energy flux. Estimates of the energy required to entrain air and the energy dissipated by bottom boundary friction were found to be too small to account for this difference. Most of the energy is therefore likely to be dissipated above the wave trough.

Turbulence acts to diffuse the bubbles throughout the water column. When the interval between successive breaking waves is less than the subsequent rise time or dissolution time of the bubbles, a persistent bubble cloud is generated. The interaction between bubbles and turbulence is also examined, and observations suggest bubbles do not have a significant effect on the turbulence.

Examiners:

Dr. D. M. Farmer, Supervisor (Institute of Ocean Sciences)

Dr. C. J. R. Garrett, Departmental Member (Department of
Physics and Astronomy)

Dr. R. Lueck, Outside Member (School of Earth and Ocean Sciences)

Dr. G. B. Deane, External Examiner (Scripps Institution
of Oceanography, La Jolla, California)

Table of Contents

Abstract	ii
Table of Contents	iii
List of Tables	v
List of Figures	vi
Acknowledgements	viii
Dedication	ix
1 Introduction	1
2 Theoretical Framework	4
2.1 An Introduction to the Surf Zone	4
2.2 Small Amplitude Linear Wave Theory	6
2.3 Isotropic Turbulence	10
2.4 Bubbles	12
2.5 Discussion	15
3 Direct Measurements	16
3.1 The Experiment	16
3.2 Sampling Space	20
3.3 The Measurements	22
3.3.1 Surface Elevation	22
3.3.2 Velocity	24
3.3.3 Air Content	28
4 Results	32
4.1 Sea State	32
4.2 Wave Energy Flux	32
4.3 Dissipation Measurements	36
4.4 Bubble Evolution	45

5	Discussion	50
5.1	Energy Considerations	50
5.1.1	Energy Loss through Bubble Entrainment	52
5.1.2	Energy Loss at the Bottom Boundary	53
5.1.3	Turbulent Kinetic Energy in the Water Column	55
5.1.4	Discussion	57
5.2	The Generation of Persistent Bubble Clouds	59
5.2.1	Processes Affecting Bubble Clouds	59
5.2.2	Scale Analysis	60
5.2.3	A Simple Model for the Turbulent Diffusion of Bubbles	61
5.2.4	The Bubble Barrier	64
5.3	A Final Look at Turbulence in the Surf Zone	69
6	Summary	73
6.1	Summary	73
6.2	Recommendations for Future Work	75
	Bibliography	76

List of Tables

3.1	Details of the instruments.	18
5.1	Frequency of wave breaking.	66

List of Figures

2.1	Schematic of plunging and breaking waves.	5
2.2	Parameters used in the development of linear theory.	7
2.3	The surface bubble pattern.	13
2.4	Bubble rise speeds.	14
3.1	(a) Bathymetry north of Scripps Pier. (b) Experimental layout.	17
3.2	The surf frame.	19
3.3	Oceanographic conditions: tide, H_s , water temperature, and salinity.	19
3.4	Instrument sampling depth.	20
3.5	Schematic of nearshore reference frames.	21
3.6	Surface displacement derived from inversion of pressure data.	23
3.7	Velocity segment before and after unwrapping.	26
3.8	Two-dimensional velocity field.	27
3.9	Combining air fraction data from two sensors.	31
4.1	Hourly significant wave heights.	33
4.2	Wave energy calculated for various wave forms.	35
4.3	Wave energy flux derived from sea surface elevation data.	36
4.4	Wave energy flux in the surf zone.	37
4.5	Spatial detrending of the velocity field.	39
4.6	Averaging the velocity spectrum.	40
4.7	Velocity spectrum noise level as a function of air fraction.	41
4.8	Histogram of spectral slopes.	42
4.9	Dissipation rate as a function of wavenumber.	43
4.10	Time series of the dissipation rate.	44
4.11	Air fraction.	45
4.12	Volume-scaled bubble size distribution.	46
4.13	Surface elevation and air fraction.	48
4.14	Evolution of the bubble size distribution.	49
5.1	Comparing dissipation rates.	51
5.2	Eddy viscosity.	58
5.3	Diffusion of bubbles within a cloud.	62

5.4	Bubble cloud width as a function of time.	63
5.5	Bubble dissolution time as a function of water saturation level.	64
5.6	Time lines of the processes affecting bubbles.	65
5.7	Backscatter from the 100 kHz sonar.	68
5.8	Decay in number of bubbles.	70
5.9	Comparing the spectral slope to the air fraction.	72

Acknowledgements

I would like to thank David Farmer for the opportunity to work at IOS. Both his guidance and generous financial support are gratefully acknowledged. I would also like to thank Chris Garrett for convincing me to leave Toronto to study on the beautiful West Coast, for his financial support, and guidance. Acknowledgements are also due to Grant Deane and Rolf Lueck for many helpful discussions.

I have enjoyed my time at IOS, and this is due in large part to those I work with. Special thanks to Grace Kamitakahara-King for all her computer help (and for letting me know about the cottage on Meldram Drive), to Christine Erbe for her moral support, to Svein Vagle for patiently answering all my questions, and to Pip Sumsion for ensuring the pay cheques kept arriving. To my fellow students, Tetjana Ross, Frank Gerdes, and Burkard Baschek, many thanks for the laughs and the words of encouragement. (I'll always have fond memories of the dinner parties!)

Last but not least, I must thank all those outside the world of oceanography who helped me through this adventure... Jill for her e-support; Ulrike for her friendship; BCTel/Telus for the great long-distance rates; and to Uta and Koit for sharing their home during the final months. To Jeff for the lessons in law (no, really!) and to grandma, grumpa, mom and dad, thank you for your never-ending love and belief in me. And finally, to Sonny, thank you for encouraging me to try something new, and waiting so patiently these past few years.

*I dedicate this thesis to my parents,
Sue and John Kendall*

1 Introduction

Waves acquire energy from open ocean winds and carry it to coastal regions, where much of the energy is released through wave breaking and decays as turbulence. The continuous approach and breaking of waves in the nearshore region generates the currents that drive sediment transport, resulting in a perpetually evolving beach morphology. Turbulence also plays a role in sediment transport. At the sea floor, turbulence generated through the interaction of the currents and the passing waves with the bottom topography lifts sediment into suspension, enabling it to be swept away by the currents.

In the middle of the water column, turbulence is diffused upward from the bottom boundary layer, and downward from the surface, where breaking waves generate stronger, less steady turbulence. Results from both laboratory [*Nadaoka et al.*, 1989] and numerical studies [*Lin and Liu*, 1998] suggest that turbulence generated by the breaking mechanism dominates in this region, and may be the dominant source even at the very bottom, as in the case of plunging breakers [*Ting and Kirby*, 1996].

Large clouds of bubbles are also generated by breaking waves. Bubbles enhance the transfer of gas between the atmosphere and the ocean [*Farmer et al.*, 1993], and persistent breaking frequently leads to supersaturation of the near surface layer [*Keeling*, 1993]. Considering the extent of wave breaking in the ocean, bubbles cannot be ignored when studying global air-sea interactions. Although the mechanisms leading

to breaking in the surf zone differ from those in deep water, the small scale processes occurring within the breaking wave crest are similar [Miller, 1976], and the mechanisms of bubble formation observed in the surf zone should also apply to the open ocean.

An understanding of the formation and evolution of bubbles is equally important when using acoustics to study the sea. At low densities, bubbles reduce the speed of sound in water [Leighton, 1994], while at large densities, acoustic signals can be completely blocked [Farmer *et al.*, 2000, accepted]. Bubble clouds have been observed to continuously block signals for up to several minutes. Bubbles also contribute to the ambient noise field in the ocean [Leighton, 1994], with sound being emitted during entrainment as well as through the collective oscillation of the bubbles.

Many researchers have recognized the direct effect turbulence has on the evolution of the bubble population, primarily in keeping the bubbles in suspension [Thorpe, 1984a; Nielsen, 1993]. Less studied is the effect bubbles have on turbulence. Nadaoka *et al.* [1989] mention that the buoyancy introduced by air bubbles is expected to influence the evolution of turbulent eddies, but found this to be beyond the scope of their laboratory study. George *et al.* [1994] speculate that bubbles present during a natural surf zone experiment may have been the cause of variations in the measured velocity spectral slopes, but were unable to confirm this without bubble measurements. Melville *et al.* [1997] also found variations in the spectral slope in a natural surf zone study. Outside the surf zone, the spectral slope clearly indicated the existence of an inertial subrange, whereas significant departures from the expected slope occurred in the presence of frequent wave breaking. Melville *et al.* [1997] suggest intermittency prevents an inertial subrange from being maintained in the surf zone. During a laboratory experiment, Pidgeon [1999] identified small turbulence structures that she believed were created by the wakes of air bubbles. However, her imaging technique was incapable of measuring the flow in the presence of bubbles, so the small structures were visible only after the bubbles had risen out of the field of view. Bubble

size measurements were not made during this experiment either.

Many studies of laboratory beaches have been performed [*Nadaoka et al.*, 1989; *Lamarre and Melville*, 1991; *Ting and Kirby*, 1996], and detailed numerical studies of breaking waves are beginning to emerge [*Lin and Liu*, 1998]. Although the results cannot always be extended to real beaches, the ability to partially isolate individual processes makes these two approaches invaluable. For instance, currents can be removed from the system, beach morphology can be controlled, and waves can be made to repeatedly break in the same location. Laboratory and numerical studies are also important because of the relatively few experiments that have been performed in the natural setting. When experiments on natural beaches are performed, they generally focus only on turbulence [*Thornton*, 1979; *George et al.*, 1994], or on bubble entrainment [*Terrill*, 1998]. Studies comprising a comprehensive set of measurements in the natural setting are still required.

This thesis is a result of such an experiment. One aim is to study the energetics of the natural surf zone through a comparison of the energy input derived from the surface wave field with the energy dissipation measured within the surf zone. The energy dissipated by the entrainment of air and bottom friction is also examined. Another aim is to provide a qualitative description of bubble-turbulence interactions and to discuss the generation of persistent bubble clouds.

Chapter 2 provides the background physics required to analyze and interpret the data. Chapter 3 describes the field experiment and data set. Energy calculations are provided in chapter 4, followed, in chapter 5, by a discussion of the results. Finally, chapter 6 summarizes the main results, and suggests directions for further study.

2 Theoretical Framework

2.1 An Introduction to the Surf Zone

Much of the energy that waves acquire from the wind as they travel across the ocean is ultimately dissipated in the nearshore region. The currents that drive sediment transport are generated by repeated wave breaking [Komar, 1998]. Turbulence is generated by individual breaking waves.

The surf zone is defined as the region shoreward of the point at which waves break. Because the incoming waves are highly irregular, and the location of initial breaking depends in part on the ratio between the trough-to-peak wave height and the water depth, no single break point exists. It is useful to calculate the significant wave height, an average of the largest one-third of the waves present [Inman *et al.*, 1971], and define the surf zone as the region shoreward of the point at which the *significant* waves break. A wave begins to break when the ratio of the wave height to water depth falls in the range 0.7 to 1.2, with the specific value depending on the deep water wave slope and the beach slope [Battjes, 1974].

Two distinct regions are present within the surf zone. Immediately following the onset of breaking, a wave undergoes a rapid and significant change in shape. This occurs in the transition region. The bore region describes the zone in which further changes to the wave are more gradual. The transition region has a cross-shore width of

approximately eight to ten water depths, while the bore region occupies the remainder of the surf zone [Svendsen, 1991]. Depending on the width of the bore region, which depends on the beach slope, the surf zone can range anywhere from tens to hundreds of metres [Miller, 1976].



Figure 2.1: *The two predominant breaker types: plunging and spilling.*

The type of breaking wave depends on the deep water wave slope (the wave height to wavelength ratio, H/λ) and the beach slope. In theory, the breaker type can be classified according to the Iribarren number,

$$\xi_0 = \frac{m}{(H_0/\lambda_0)^{1/2}}, \quad (2.1)$$

where m is the beach slope, and the subscript “0” denotes deep water wave properties [Battjes, 1974]. The two most frequently observed breaker types are illustrated in Figure 2.1. Surging breakers, with $\xi_0 > 3.3$ [Battjes, 1974], tend to occur on beaches with the steepest slope, although since the collapsing wave surges up the beach face, a surf zone through which bores propagate does not exist. Plunging breakers, with $0.5 < \xi_0 < 3.3$ [Battjes, 1974], occur most frequently on steeply sloping beaches, resulting in narrow surf zones [Thornton, 1979]. In contrast, spilling breakers, with $\xi_0 < 0.5$ [Battjes, 1974], tend to occur on beaches with mild to intermediate slopes, where the waves exist as bores for a much longer period of time. The energy in the spilling breaker is therefore lost at a slower rate over a larger area than in the case of the plunging breaker [Komar, 1998].

Lin and Liu [1998] divide the wave breaking process into three distinct stages. The first stage is characterized by irrotational flow [*Battjes*, 1988] as the wave height increases and the forward face of the wave steepens and overturns. The flow becomes rotational during the second stage when the overturning crest impinges on the wave trough. As a result of the vortices and turbulence that are generated, the wave experiences a rapid transition in shape, including a sharp decrease in height. The final stage of breaking occurs farther shoreward, where the wave evolves more slowly as a turbulent bore.

The mechanisms just described occur in both spilling and plunging breakers, although at different size scales [*Miller*, 1976; *Thornton*, 1979]. At larger scales, the crest jets out and plunges into the wave base, creating an initial vortex with a length scale on the order of the water depth. Splashing may also generate a succession of additional vortices of decreasing strength. At smaller scales, the jet is weak, and appears to spill down the face of the wave, creating much weaker vortices that tend not to extend beneath the wave trough. Natural breaking waves exist as a gradation between these extremes, with properties intermediate between the two.

From photographs of entrained laboratory bubbles, *Nadaoka et al.* [1989] determined that the eddies created by wave breaking fall into two types: horizontal eddies parallel to the wave crest and obliquely descending eddies trailing the crest. Since the multiple horizontal eddies created by a single breaking wave all rotate in the same direction, a high rate of energy dissipation must exist in the region between the successive eddies where the shear rate is high [*Battjes*, 1988].

2.2 Small Amplitude Linear Wave Theory

As a result of the changing water depth, waves approaching the nearshore region undergo a transformation in shape. In contrast to the fairly sinusoidal deep water waves, waves in water of intermediate to shallow depths have sharper peaks separated

by wider, flatter troughs. Many theories have been developed to model nearshore waves, including cnoidal wave theory, solitary wave theory, and high order Stokes wave theory. *Sarpkaya and Isaacson* [1981] provide a nice description and summary of results for each of the theories.

Linear theory provides the simplest description of waves. Since it describes monochromatic sinusoids perfectly, linear theory can be applied to the individual Fourier components of any wave train. Linear theory is based on the following assumptions: the water is incompressible and inviscid; the flow is irrotational; and locally, the bottom is horizontal. Small amplitude theory further requires that the amplitude of the wave is much less than both the wavelength and the water depth. Figure 2.2 illustrates the parameters and coordinate system used in the following somewhat abridged discussion of linear theory, which can be found in greater detail in many texts (see, for example, *Kundu* [1990], *Sarpkaya and Isaacson* [1981], or *Dean and Dalrymple* [1991]).

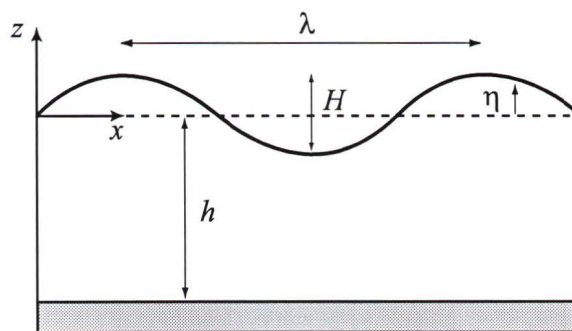


Figure 2.2: Parameters used in the development of linear theory. (The figure is not drawn to scale.)

For an irrotational flow, a velocity potential, ϕ , can be defined such that

$$u \equiv \frac{\partial \phi}{\partial x}, \quad w \equiv \frac{\partial \phi}{\partial z}, \quad (2.2)$$

where u and w are the horizontal (in the direction of wave propagation) and vertical

velocity components, respectively. For an incompressible fluid, it follows that

$$\frac{\partial u}{\partial x} + \frac{\partial w}{\partial z} = 0. \quad (2.3)$$

Substituting equation (2.3) into (2.2) yields Laplace's equation,

$$\frac{\partial^2 \phi}{\partial x^2} + \frac{\partial^2 \phi}{\partial z^2} = 0, \quad (2.4)$$

which is subject to the bottom boundary condition

$$\frac{\partial \phi}{\partial z} = 0 \quad \text{at } z = -h. \quad (2.5)$$

To first order, the small-amplitude kinematic surface boundary condition is

$$\frac{\partial \phi}{\partial z} = \frac{\partial \eta}{\partial t} \quad \text{at } z = 0, \quad (2.6)$$

and the dynamic surface boundary condition is

$$\frac{\partial \phi}{\partial t} = -g\eta \quad \text{at } z = 0, \quad (2.7)$$

where g is the acceleration due to gravity. The wave is assumed to be a simple sinusoid represented by

$$\eta = \frac{H}{2} \cos(kx - \omega t), \quad (2.8)$$

where k is the wavenumber, and ω is the angular wave frequency.

Applying boundary conditions (2.6) and (2.7) to the Laplace equation (2.4), the velocity potential is found to be

$$\phi = \frac{H}{2} \frac{\omega}{k} \frac{\cosh k(z+h)}{\sinh kh} \sin(kx - \omega t). \quad (2.9)$$

From the definition of the velocity potential (2.2), it follows that the water particle velocities are given by

$$u = \frac{H}{2} \omega \frac{\cosh k(z+h)}{\sinh kh} \cos(kx - \omega t) \quad (2.10)$$

and

$$w = \frac{H}{2} \omega \frac{\sinh k(z+h)}{\sinh kh} \sin(kx - \omega t). \quad (2.11)$$

The linear dispersion relation,

$$\omega = \sqrt{g k \tanh kh}, \quad (2.12)$$

is found by substituting the velocity potential (2.9) into (2.7), and can be used to calculate the phase speed, $c = \omega/k$.

The energy of the wave is composed of kinetic energy resulting from the motion of water particles at all depths, and potential energy resulting from the rise and fall of the water surface. The kinetic energy, averaged over the wave length and integrated over the water column, is given by

$$KE = \frac{1}{2} \frac{\rho}{\lambda} \int_0^\lambda \int_{-h}^0 (u^2 + w^2) dz dx, \quad [J m^{-2}] \quad (2.13)$$

which, using equations (2.8), (2.10) and (2.11), can be simplified to

$$KE = \frac{1}{2} \rho g \overline{\eta^2}, \quad [J m^{-2}] \quad (2.14)$$

where $\overline{\eta^2} = \frac{1}{\lambda} \int_0^\lambda \eta^2 dx$. The potential energy is given by

$$PE = \rho g \frac{1}{\lambda} \int_0^\lambda \int_0^\eta z dz dx. \quad [J m^{-2}] \quad (2.15)$$

Upon simplification of (2.15), the total energy density, $E_{tot} = KE + PE$, is found to be equally partitioned between kinetic and potential,

$$KE = PE = \frac{1}{2} \rho g \overline{\eta^2}. \quad [J m^{-2}] \quad (2.16)$$

The energy is transported by the wave at the group speed, defined as $c_g \equiv d\omega/dk$.

As mentioned at the beginning of the section, waves undergo a transformation as they enter the nearshore region. The nonlinear steepening of shoaling waves results in amplitudes that are on the order of the water depth, so that *small-amplitude* linear theory is no longer applicable. However, rather than applying the more complex, higher-order theories, a good approximation to the small-amplitude theory can be

obtained by substituting equation (2.8) with the real wave field. Writing the surface wave field as

$$\eta(t) = \sum_n A_n \cos(-\omega_n t + \phi_n), \quad (2.17)$$

the amplitude, A_n , and the phase, ϕ_n , of each component, n , can be determined from Fourier decomposition of the time series. Then, for example, the horizontal velocity can be computed from

$$u(t) = \sum_n A_n \omega_n \frac{\cosh k_n(z+h)}{\sinh k_n h} \cos(-\omega_n t + \phi_n). \quad (2.18)$$

He [1997] describes the numerical steps involved in applying Fourier theory to a time series of surface elevation.

As will be seen later, the velocity and the wave energy can be successfully calculated when the experimentally measured wave field is applied as the surface boundary condition since no attempt is made at predicting the evolution of the wave train.

2.3 Isotropic Turbulence

*Big whirls have little whirls that feed on their velocity,
and little whirls have lesser whirls and so on to viscosity.*
- Lewis Fry Richardson¹

Turbulent flows occur at many different scales, from kilometre sized atmospheric boundary layer flows, to centimetre sized flows in the surf zone. A wide range of scales also exists within a single turbulent flow, with eddies ranging from a size on the order of the width of the flow, down to the smallest viscous scale. The input of energy generally occurs at the largest scales, and is subsequently transferred to smaller and smaller scales until it is lost to viscous dissipation. In order for turbulence to be maintained, a continuous input of energy must therefore exist. Although many

¹Richardson wrote this poem [Richardson, 1965] to summarize his 1920 paper entitled “*The supply of energy from and to Atmospheric Eddies*”.

flows are random and highly nonlinear, it is this dissipative nature of turbulence that distinguishes it from other irregular flows.

Energy is extracted from the mean flow by the largest eddies and is dissipated by the smallest. At all intervening scales, energy is neither produced nor destroyed, but rather “cascades” from larger to smaller scales.² According to Kolmogorov’s theory, the inertial subrange is the range of wavenumbers within the cascade where the flow is isotropic, and the energy spectrum is independent of both the large scale energy-containing eddies and the viscosity. Within the inertial subrange, the three-dimensional energy spectrum is dependent only on the rate of energy transfer across the range, and therefore on the dissipation rate, and is found by dimensional arguments to be

$$\Phi(k) = A\varepsilon^{2/3}k^{-5/3}, \quad (2.19)$$

where ε is the rate of dissipation, k is the wavenumber, and $A = 1.5$ is a universal constant, valid for all turbulent flows [Kundu, 1990]. For isotropic turbulence, the relation between the three-dimensional spectrum, $\Phi(k)$, and the one-dimensional spectrum of the longitudinal velocity fluctuations, $\phi_1(k)$, is given by Hinze [1975] as

$$\Phi(k) = \frac{1}{2}k^2\frac{\partial^2\phi_1}{\partial k^2} - \frac{1}{2}k\frac{\partial\phi_1}{\partial k}. \quad (2.20)$$

Substituting equation (2.19) into (2.20), the one-dimensional spectrum is found to be

$$\phi_1(k) = \frac{18}{55}\Phi(k). \quad [m^3 s^{-2}] \quad (2.21)$$

The spectrum of the transverse velocity fluctuations is related to the spectrum of the longitudinal velocity fluctuations by $\phi_2 = \frac{4}{3}\phi_1$.

The inertial subrange occurs in the range

$$l^{-1} \ll k \ll \eta^{-1}, \quad (2.22)$$

²Tennekes and Lumley [1972] provide a nice qualitative description of the cascade in terms of a waterfall analogy. Lewis Fry Richardson also captured the essence of this concept in the poem quoted at the beginning of this section.

where l is a typical length scale of the largest eddies, and the Kolmogorov microscale,

$$\eta \equiv \left(\frac{\nu^3}{\varepsilon} \right)^{1/4}, \quad (2.23)$$

is the length scale of the smallest eddies. An order of magnitude estimate for the dissipation rate is given by

$$\varepsilon \sim \frac{u'^3}{l}, \quad (2.24)$$

where u' is a typical scale for the turbulent velocity fluctuations. Inserting equation (2.24) into (2.23), and defining the turbulent Reynolds number as $Re \equiv \frac{Ul}{\nu}$, where U is a velocity scale of the largest eddies,

$$\frac{\eta}{l} \sim Re^{-3/4}. \quad (2.25)$$

A necessary condition for the occurrence of an inertial subrange is therefore a high Reynolds number flow [Tennekes and Lumley, 1972]. The larger the Reynolds number, the greater the size difference between the energy-containing eddies and the eddies at which the energy is dissipated, and the broader the inertial subrange. According to Tennekes and Lumley [1972], a “sufficiently large” Reynolds number is $Re \gg 10^5$, which corresponds to $l/\eta \gg 10^3$.

2.4 Bubbles

Oceanic bubbles are generated by many mechanisms, including the impact of rain on the ocean surface and biological sources. The primary source of bubbles near the ocean surface is wave breaking [Monahan, 1993]. Following a breaking event, bubbles are arranged into plumes. By comparing photographs taken above the waves to underwater images, Deane [1997] determined that the foam patterns at the sea surface are an approximate map of the location of the underwater plumes. Figure 2.3, a photo taken from Scripps Pier in May 1999, illustrates the initial plumes, which, as observed by Deane [1997], tend to lie in lines parallel to the wave front.



Figure 2.3: *A photo taken from Scripps Pier in May 1999, illustrating the near-surface pattern of bubbles trailing a breaking wave.*

Deane and Stokes [1999] used optical techniques to study the mechanisms of air entrainment and bubble formation in the first few seconds following wave breaking in a natural surf zone. They observed two primary mechanisms responsible for bubble creation. First, cavities of air trapped beneath the falling wave crest deform and split into bubbles. Second, the overturning jet forces long, thin filaments of air into the water at the point where the jet crashes into the wave front, and these subsequently break up to form bubbles. Larger bubbles are rapidly broken down into smaller bubbles by turbulent pressure fluctuations [*Garrett et al.*, 2000]. By examining successive images, *Deane and Stokes* [1999] determined that most bubbles are formed within the first 100 *ms* following the impingement of the crest into the wave front.

After initial formation, the bubble size distribution undergoes both a temporal and a spatial evolution as the bubbles dissolve, rise buoyantly to the surface, and advect in the presence of turbulence and background currents. The dynamics of individual bubbles depend in part on both the bubble radius and the properties describing the boundary between the gas inside the bubble and the surrounding water. Sea water contains organic impurities that accumulate on the bubble wall to form a complete surrounding “skin” within tens of seconds following bubble formation [*Thorpe*, 1982].

Bubbles around which a skin has formed are called “dirty” bubbles to distinguish them from “clean” bubbles that lack a coating. The walls of dirty bubbles have a greater ability to withstand a stress, so the bubbles behave dynamically as rigid bodies. The surface coatings also reduce the rate at which the bubbles dissolve [Leighton, 1994].

The buoyant rise speed of a bubble depends on its shape. For the bubbles considered later, with radii less than $300 \mu m$, surface tension prevents any departure from the spherical shape from being very large [Thorpe, 1982]. The rise speed can then be found by balancing the buoyancy force with the drag force,

$$\rho g \frac{4}{3} \pi a^3 = C_D \pi a^2 \frac{1}{2} \rho w_b^2, \quad (2.26)$$

where a is the bubble radius, w_b is the rise speed, and C_D is the drag coefficient [Keeling, 1993]. In terms of the bubble Reynolds number, $Re = \frac{2aw_b}{\nu}$, the drag coefficient for creeping flow around a smooth sphere is $C_D = 24/Re$. Rise speeds obtained with this value are illustrated in Figure 2.4.³

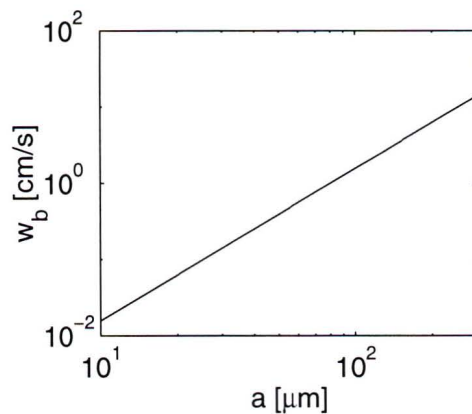


Figure 2.4: Bubble rise speeds due to buoyancy.

The dissolution of a bubble depends on both its size and the state of the boundary wall. In order to balance the additional pressure resulting from the surface tension,

³The values illustrated in Figure 2.4 correspond more closely with Figure 1 in Keeling [1993] than the speeds obtained with the C_D reportedly used by that author, $C_D = \frac{24}{Re} (1 + 0.566 \sqrt{Re})^{-1/2}$!

the internal pressure of a bubble at rest, p_i , must be greater than the pressure in the surrounding liquid, p_L [Leighton, 1994],

$$p_i = p_L + \frac{2\gamma}{a}, \quad (2.27)$$

where γ is the surface tension. As a result of the excess pressure, the partial pressure of gas within the bubble is usually greater than in the surrounding water, and the bubble will tend to dissolve. As the bubble dissolves, the radius decreases, which, by equation (2.27), increases the excess pressure, and the bubble will continue to dissolve. In the case of dirty bubbles, the skin eventually restricts the decrease in surface area, impeding further dissolution.

2.5 Discussion

From the discussion in this chapter, a qualitative description of the processes occurring during wave breaking can be formulated. Energy is transferred from the breaking wave into the water column, generating the eddies that decay into turbulence. The energy is transferred to increasingly smaller scales, eventually being dissipated as heat.

The collapsing wave crest also injects bubbles into the water column. The evolution of the bubble size distribution is determined by a number of factors. The buoyancy force tends to shift the peak in the volume-scaled size distribution to smaller radii as the largest bubbles are the first to disappear at the surface. Turbulent diffusion mixes the bubbles throughout the water column, and therefore acts to delay the surfacing of the bubbles.

Initially, the number of small bubbles will remain nearly constant with dissolving bubbles replenishing the disappearing small bubbles. However, dissolution of the smallest bubbles is impeded as they acquire surface-active materials. Persistent bubble clouds will be generated if wave breaking occurs frequently enough for a sufficient number of the bubbles to remain in suspension from one event to the next.

3 Direct Measurements

3.1 The Experiment

Between 1-14 March 1997, the Acoustical Oceanography Research Group from the Institute of Ocean Sciences (IOS) participated in a collaborative experiment near Scripps Pier, La Jolla, California, to study the effects of bubbles on high frequency acoustic propagation. Investigators from the Marine Physical Laboratory at Scripps Institution of Oceanography (SIO), the Naval Research Laboratory, the Applied Physics Laboratory at the University of Washington, and the National Center for Physical Acoustics also participated in the experiment.

Instruments were deployed in the water to the north of both the seaward and shoreward ends of the pier. The bathymetry 32 *m* north of the pier is illustrated in Figure 3.1a.¹ The general layout of the instruments is illustrated in Figure 3.1b, and Table 3.1 provides a summary of the instruments.

A CTD and five 100 *kHz* Doppler side-scan sonars were fixed to the piling at the seaward end of the pier. The sonars were directed horizontally towards the surf zone (only two of the beams are illustrated in the figure). A permanent installation of the Army Corps of Engineers (ACE) measuring wave height and period was also located at the seaward end of the pier.

¹Coastal Environments was contracted by the SIO group to survey the bathymetry on 17 February, 1997 [Terrill, 1998].

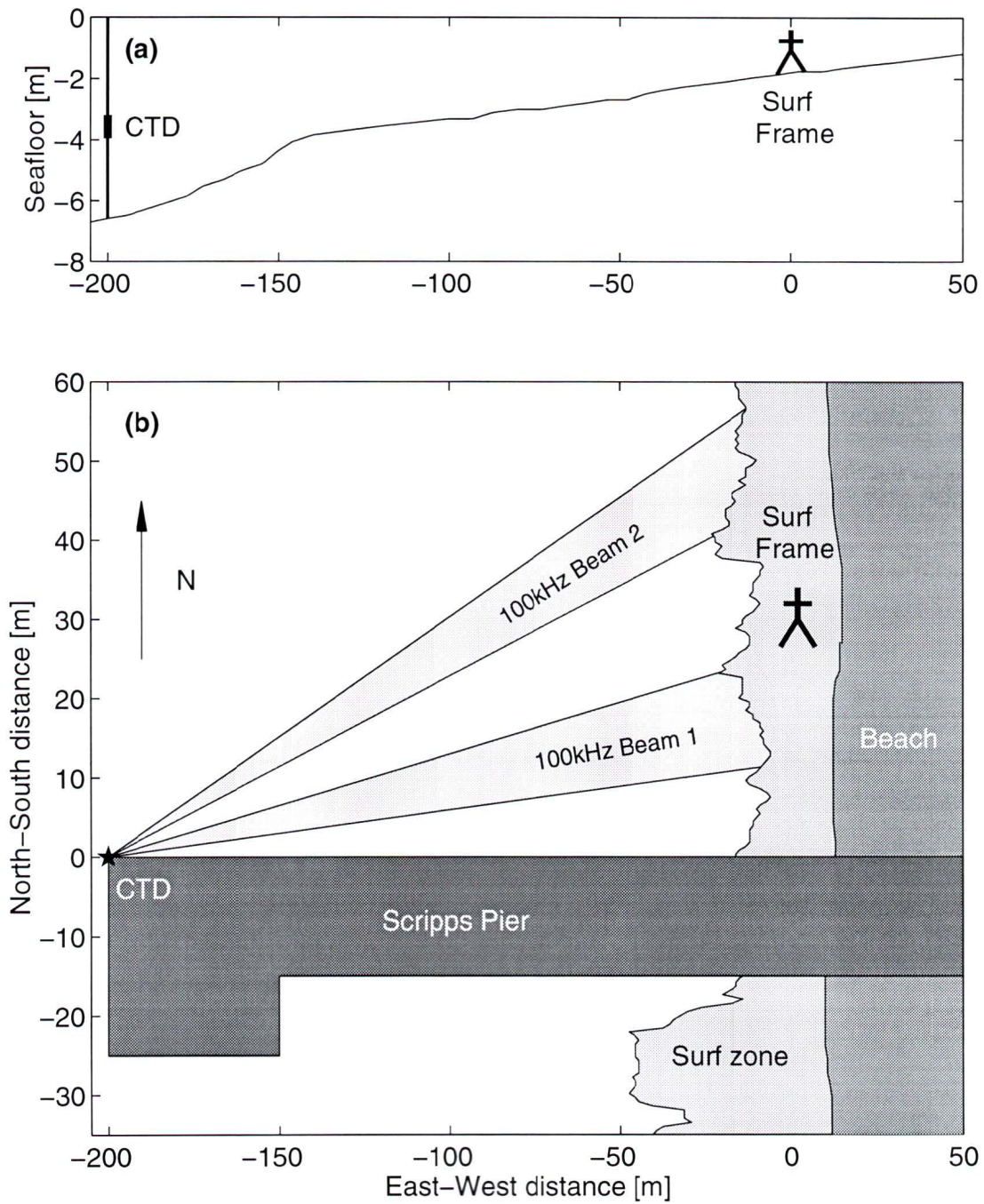


Figure 3.1: (a) Bathymetry 32m north of Scripps Pier when the mean water depth at the surf frame was 2m. (b) Layout of the instruments during the 1997 experiment.

Instrument	Location	h [m]	f_s [Hz]
100 kHz	pier	5	2
ACE pressure	pier	2.5	1
CTD	pier	3	0.02
Dopbeam	surf	1.75	40
Pressure	surf	0.5	4
Resonator	surf	1.5	2

Table 3.1: Location (where ‘surf’ denotes the surf frame), height above the sea floor, and sampling frequency of the instruments.

Within the surf zone, a frame supporting a number of instruments was fixed to the sea floor (Figure 3.2). The frame was installed during low tide, and was able to record data only once the tide was high enough to fully submerge the instruments. The instruments supported by the frame included a pressure sensor, an acoustical resonator, a thermistor, a conductivity cell, a coherent Doppler, and an underwater video camera.

The tide was predominantly semi-diurnal, resulting in two surf zone measurement periods per day. The hourly mean water depth, significant wave height, salinity, and water temperature at the seaward end of the pier are illustrated in Figure 3.3.

At the seaward end of the pier, the slope is approximately 1:25, and decreases to 1:70 approximately 50 *m* farther shoreward (Figure 3.1a). Using this gentle slope, which remains constant throughout the entire surf zone, and the deep water wave properties derived from the pier-end measurements, the Iribarren number was found to fall in the range $0.08 \leq \xi_0 \leq 0.46$. The spilling breaker should therefore be the dominant breaker type; indeed, this is what was observed in the video that was taken from the pier during the experiment.

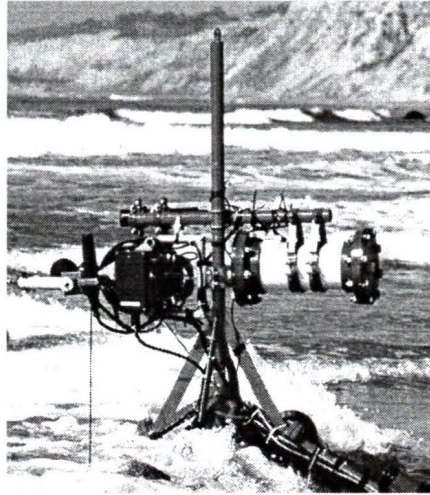


Figure 3.2: Photo of the frame installed in the surf zone. The coherent Doppler and the acoustical resonator are visible in the photo.

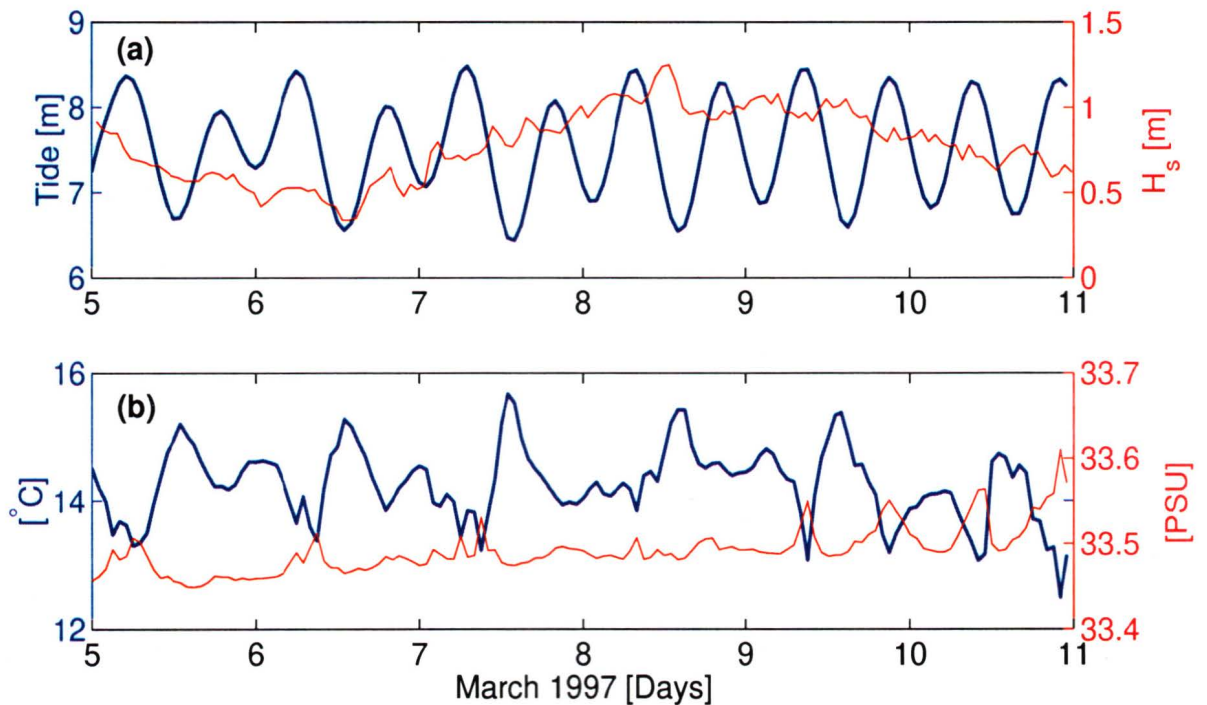


Figure 3.3: Oceanographic conditions at the seaward end of the pier during the experiment. (a) The tide measured by the CTD and the hourly significant wave height measured by the ACE pressure sensor. (c) Hourly water temperature and salinity measured by the CTD.

3.2 Sampling Space

An interesting feature of measurements obtained in the nearshore region from a stationary platform is the simultaneous spatial information that is provided by a time series. As seen in Figure 3.4a, the instantaneous water depth changes by a significant fraction of the mean water depth with each passing wave. Figure 3.4b illustrates the variable sampling depth of the instrument.

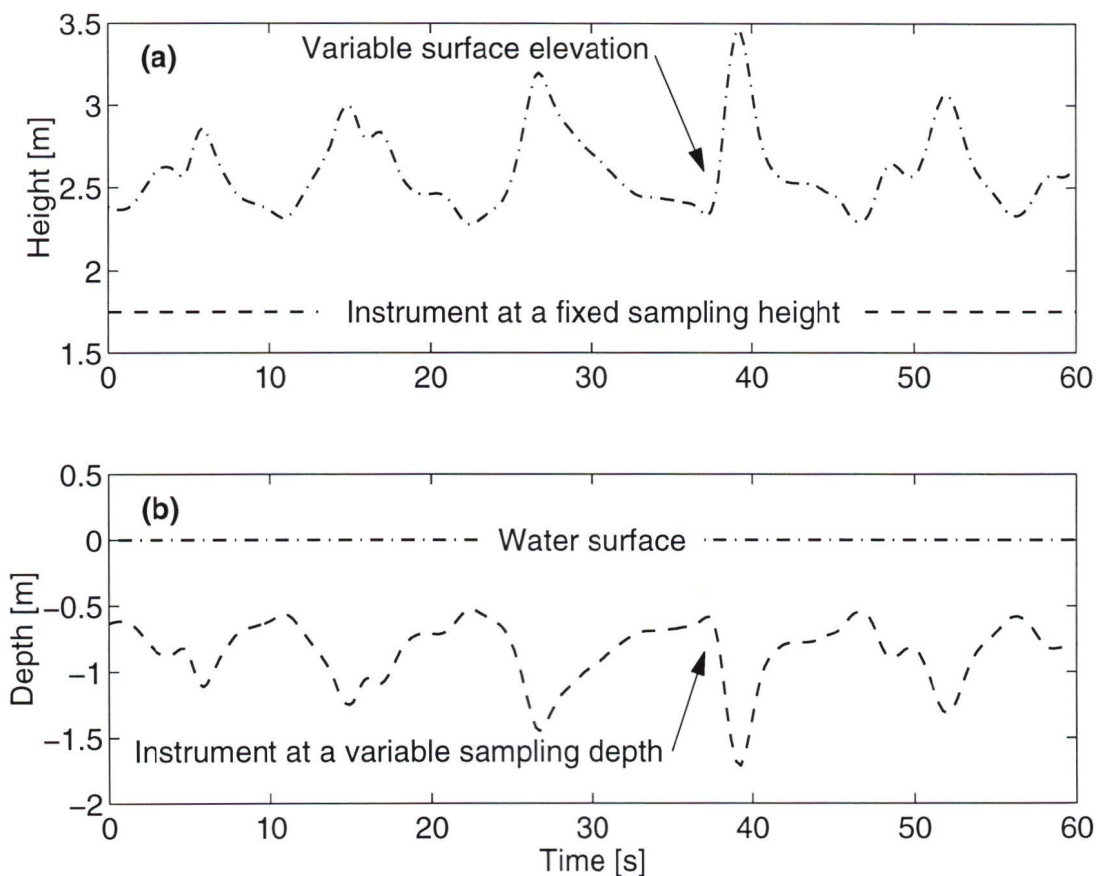


Figure 3.4: (a) The natural reference frame where heights are measured with respect to the sea floor. The instrument samples at a fixed height above the sea floor while the surface elevation changes with each passing wave. (b) A frame of reference where depths are measured with respect to the water surface. The instrument effectively samples at variable depths. Start time: 9 March 1997 22:00:11.

Over longer time scales, the mean water depth changes with the changing tide, as illustrated in Figure 3.5a. By changing the frame of reference to one where the mean water level is fixed, as in Figure 3.5b, it is clear that the instruments sample different regions of the surf zone. At the peak of high tide, the frame is located seaward of the surf zone. As the tide recedes, the frame gradually passes through the surf zone before eventually becoming exposed.

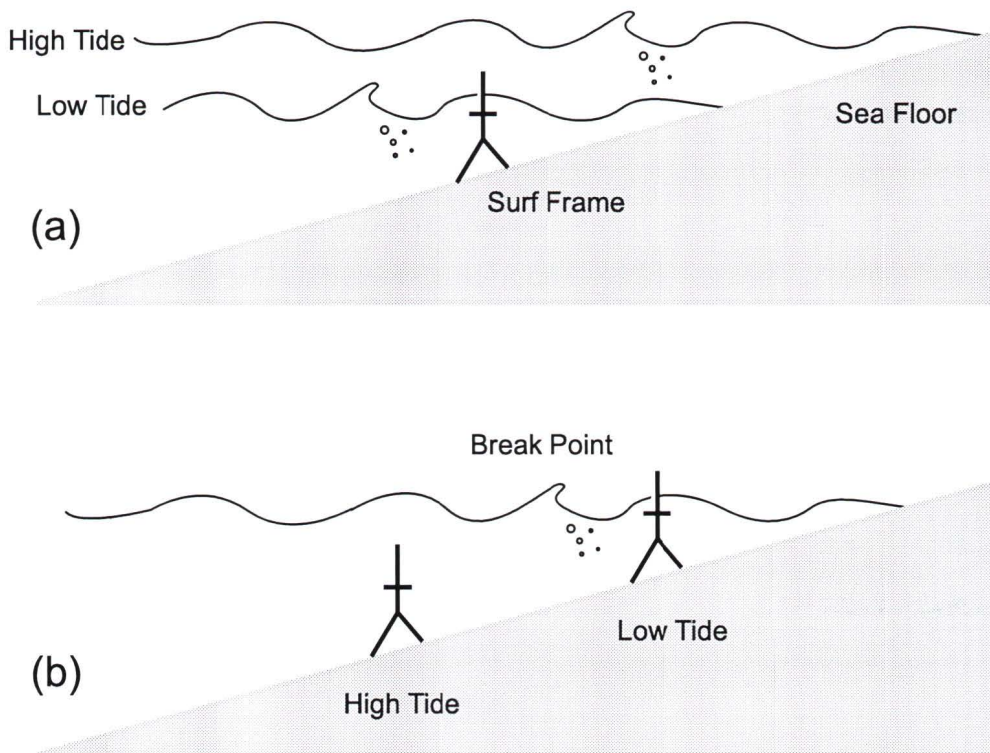


Figure 3.5: Schematic of the surf zone illustrating two different frames of reference. (a) Temporal measurements obtained by instruments sampling at a fixed location in the presence of a changing tide. (b) Spatial measurements obtained by instruments sampling different regions of the surf zone as a result of the changing water depth.

One consequence of this second form of spatial sampling is that a time series measurement obtained at a fixed location can be transformed into a function of horizontal distance. From Figure 3.1a, the slope of the seafloor is nearly constant in the vicinity

of the surf frame. Using the relation,

$$m = \frac{\Delta h}{\Delta x}, \quad (3.1)$$

where m is the beach slope, the local mean depth, h , can be transformed to a corresponding horizontal spatial variable, x . Taking measurements as a function of the new variable, spatial gradients can then be computed. This method will be applied in the next chapter to obtain the dissipation rate from the wave energy flux.

3.3 The Measurements

3.3.1 Surface Elevation

The pressure was measured at the seaward end of the pier and within the surf zone. Following *Kundu* [1990] in applying linear theory to the Bernoulli equation, the total pressure recorded by a transducer,

$$p = -\rho g z + \rho g \eta \frac{\cosh k(z+h)}{\cosh kh}, \quad (3.2)$$

is the sum of a hydrostatic component and a dynamic component resulting from the vertical accelerations generated by the passage of waves. The dynamic component tends to enlarge the wave beyond the hydrostatic case by stretching both the crest and the trough. Figures 3.6a and 3.6b compare the hydrostatic case, $\eta = \frac{1}{\rho g}(p + z)$, to the full inversion of equation (3.2),

$$\eta = \frac{1}{\rho g} \frac{\cosh kh}{\cosh k(z+h)} (p + \rho g z), \quad (3.3)$$

for theoretical sinusoids in deep and shallow water, respectively. Typical values for the wave properties were used to construct the sinusoids. The magnitude of the dynamic effect decreases with decreasing water depth.

In the shallow water limit ($\frac{h}{\lambda} \ll 1$), the pressure field is completely hydrostatic. According to *Kundu* [1990], the limit is a very good approximation for $h < 0.07\lambda$.

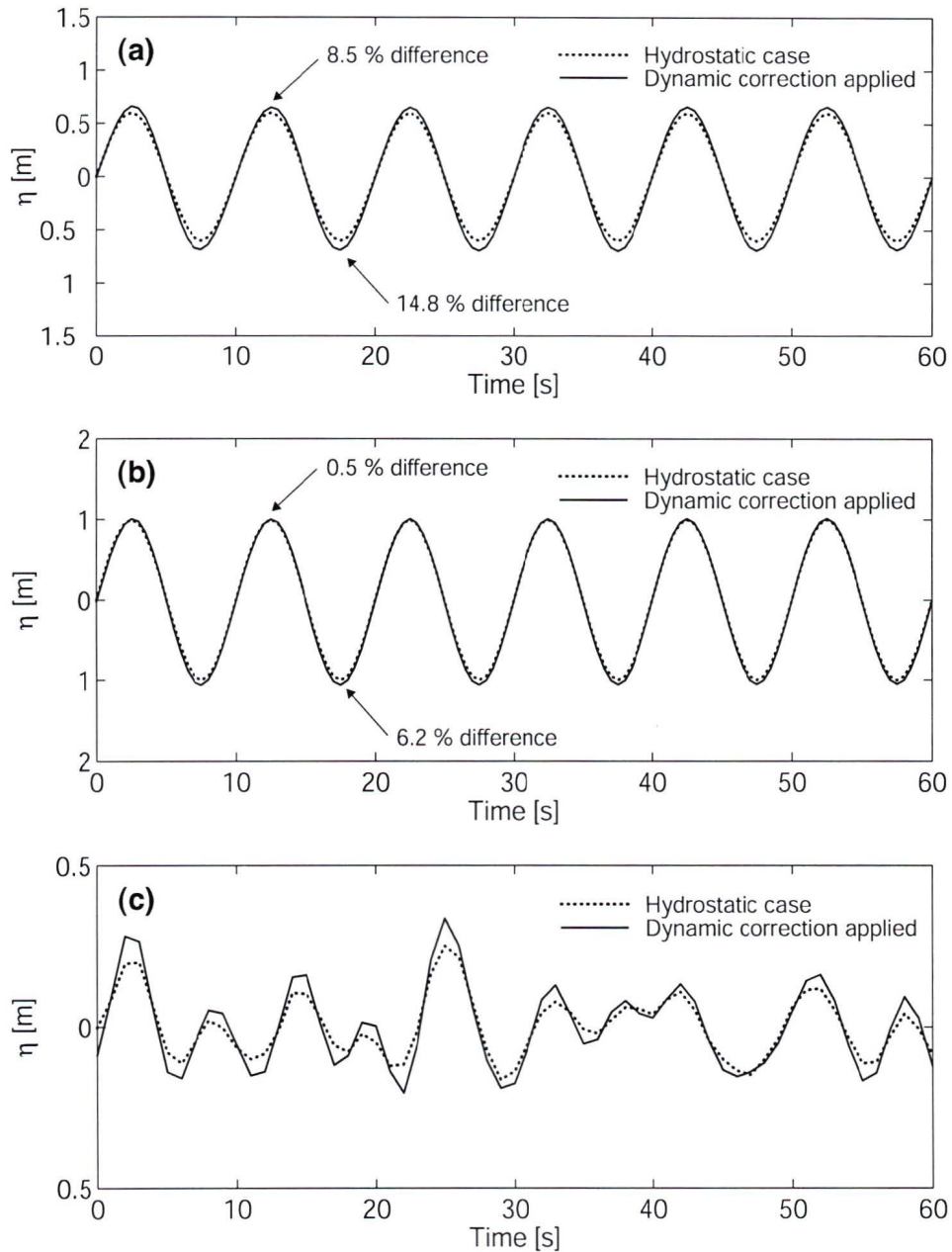


Figure 3.6: Surface displacement derived from the inversion of pressure data. (a) Theoretical sinusoid for a typical wave at the end of the pier; $h = 7.5$ m. (b) Theoretical sinusoid for a typical (non-breaking) wave within the surf zone; $h = 2.0$ m. (c) A real pier-end segment; $h = 7.3$ m; start time: 5 March 1997 23:15:00.

Within the surf zone during the experiment, typical values for h and λ were 2 m and 35 m, respectively, yielding $\frac{h}{\lambda} = 0.06$. The pressure field within the surf zone was therefore sufficiently hydrostatic for $\eta = \frac{1}{\rho g}(p + z)$ to be used to obtain the surface wave field directly from the pressure measurements.

In the deeper water at the end of the pier, typical values for h and λ were 6 m and 45 m, respectively, yielding $\frac{h}{\lambda} = 0.13$. Equation (3.2) must therefore be inverted in order to obtain the surface wave field from the pressure data [Wang *et al.*, 1986]. Differences of up to 10 cm from the hydrostatic case can be observed in Figure 3.6c.

3.3.2 Velocity

High resolution measurements of the velocity field in the surf zone were obtained with a 1.72 MHz Sontek coherent Doppler sonar. Despite problems with the processing scheme that resulted in useful data being collected only in five minute segments at near-hourly intervals, various phases of the tide were sampled, and velocity measurements were obtained in the presence and absence of frequent wave breaking.

From 5-6 March, the sonar faced the incoming waves in a cross-shore orientation, while from 7 March until the end of the experiment, the orientation was longshore. Turbulent velocity fluctuations were measured in both cases: while in the cross-shore orientation, they were superimposed on the wave orbital field and rip currents; while in the longshore orientation, they were superimposed on longshore currents. The approach of the incoming waves was predominantly normal to the beach. However, since the instantaneous direction of the incoming waves will depend on the local seafloor topography, the velocity measurements obtained while in the longshore orientation may contain a small wave orbital component.

The pulse-to-pulse coherent Doppler sonar transmits a series of short pulses and observes the change in phase of backscatter between successive transmissions, with each return representing a different range bin [Zedel *et al.*, 1996]. Although it is particles in the water, not the fluid, that cause the backscatter, sand grains can be

treated as passive tracers if the particle response time is less than the Kolmogorov time microscale. The particle response time is defined as $\tau_p = w_s/g$, where w_s is the still-water settling velocity [Zedel and Hay, 1999]. At the beach near Scripps Pier, the sand grains ranged in size from 200 – 500 μm [Deane, 1997]. With settling velocities in the range 25 – 70 mms^{-1} [Fredsoe and Deigaard, 1992], the sand particles have response times of 2 – 7 ms . Since the Kolmogorov microscale, $\tau_K \equiv \left(\frac{\nu}{\varepsilon}\right)^{1/2}$, is on the order of 30 ms , the particles present during the experiment can be assumed to move passively through the water.

The radial velocity is derived from the Doppler relation,

$$V = \frac{c}{4\pi f} \frac{d\phi}{dt}, \quad (3.4)$$

where c is the speed of sound in water, f is the sonar frequency, and $\frac{d\phi}{dt}$ is the phase rate of change. When the change in phase is greater than 180° , an aliased velocity is measured. The resulting time series is “wrapped” about zero, bounded above and below by the maximum unambiguous velocity,

$$V_{max} = \pm \frac{c}{4f\tau}, \quad (3.5)$$

where τ is the time between successive pulses. The velocities are “unwrapped” according to the scheme described by He [1997]. Figure 3.7 compares a short velocity time series before and after the ambiguity has been resolved.

The unwrapping scheme assumes the backscatter remains coherent between successive transmissions. The advection of particles into and out of the sample volume, turbulence-induced random scatterer motion, and beam divergence all contribute to decorrelation [Cabrera et al., 1987]. Although the effect of beam divergence is small, since the angular width of the beam is only 1.5° [Zedel and Hay, 1999], a loss of coherence is expected as a result of the rapidly changing velocity field immediately following a breaking event. Fortunately, for the analysis of the turbulence field, the essential step is spatial unwrapping, an inherently more robust procedure than the temporal unwrapping.

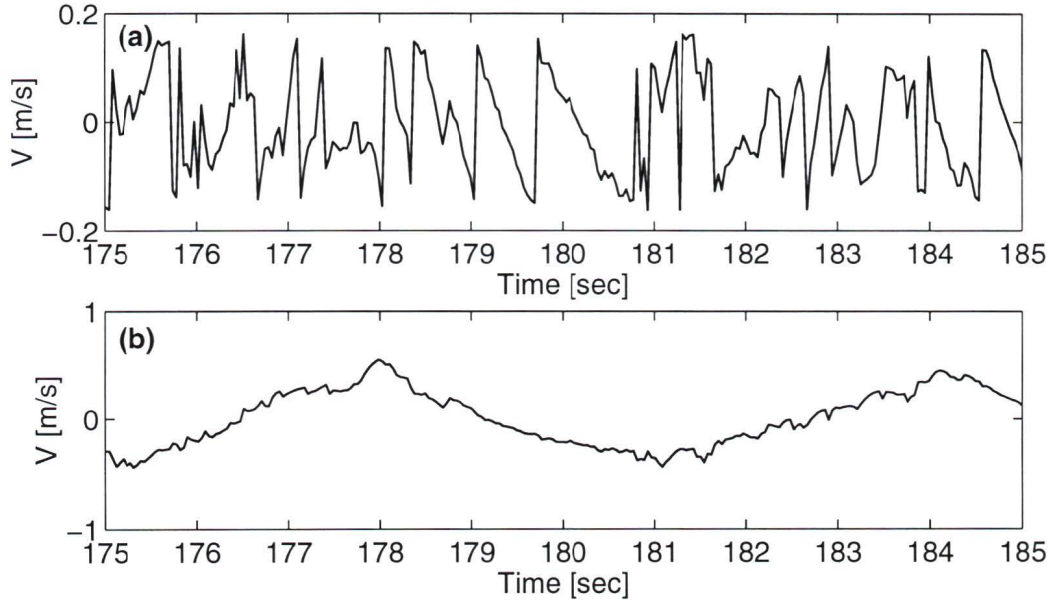


Figure 3.7: (a) Sample of wrapped data. (b) The same segment of data after the unwrapping procedure has been applied. The cross-shore velocities are at 0.5 m from the instrument. Start time: 6 March 1997 19:35:09.

The coherent Doppler samples the two-dimensional velocity field. Figure 3.8a compares the velocity extracted at a single range to the orbital velocity obtained by applying linear theory to the surface elevation. The measured velocity is the superposition of the turbulent fluctuations on the orbital velocity. In the two-dimensional velocity field in Figure 3.8b, the alternating bands of blue and red highlight the dominant orbital velocity component, and the fine scale modulation is the turbulence.

The turbulence, defined here as the velocity that remains after linear spatial detrending, is illustrated in Figure 3.8c. (See section 4.3 for further discussion of the detrending method.) Coherent structures of varying sizes are clearly visible. These are advected through the sampling region by the orbital velocity. Where the advection of smaller eddies is not in phase with the orbital movement of the water, such as at $t \approx 134$ s, the advection may be caused by large scale eddies or by vertical motions that cannot be resolved by the instrument.

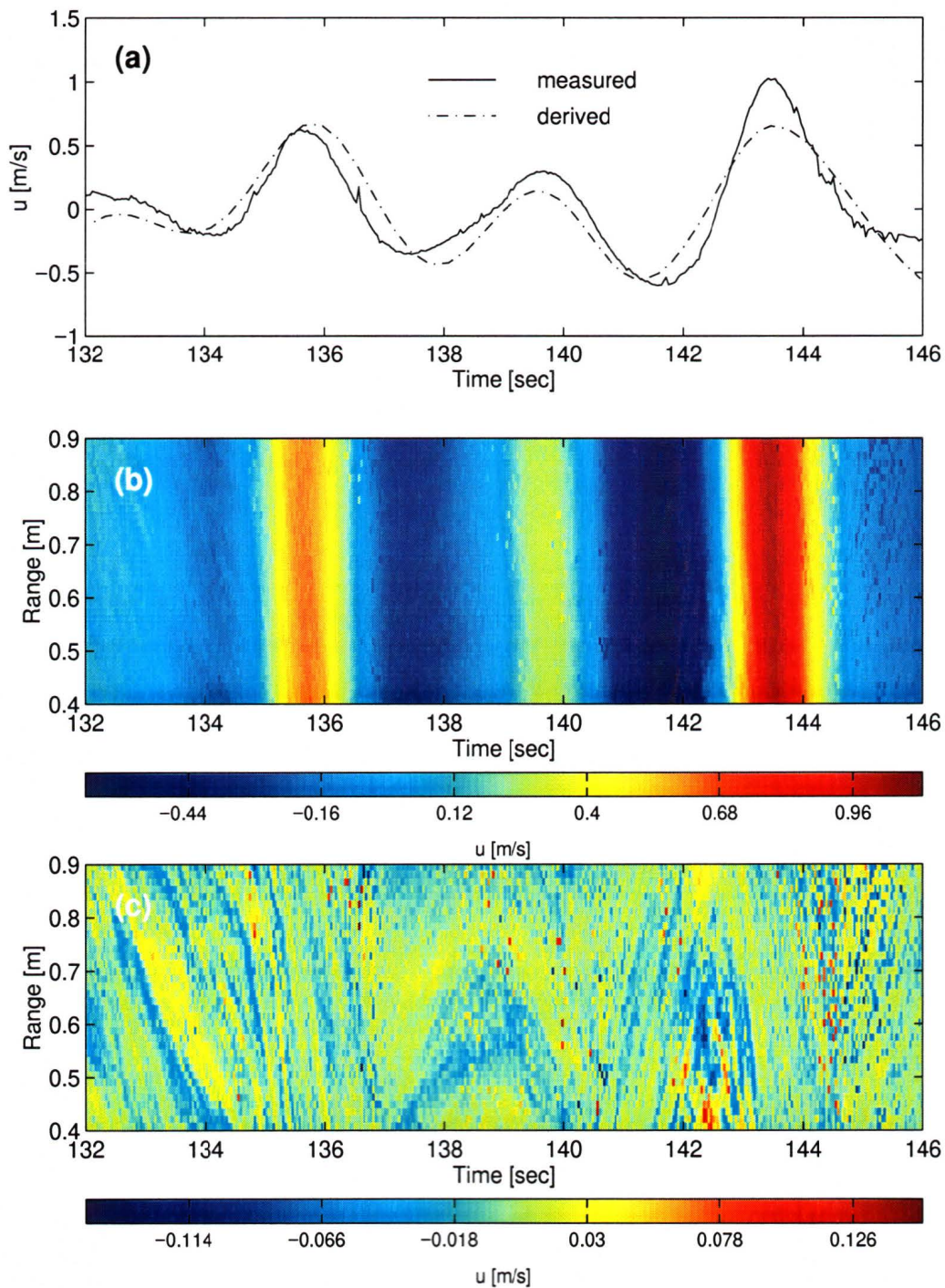


Figure 3.8: (a) The orbital velocity derived from the surface elevation and the velocity measured 0.8 m from the sonar. (b) The velocity field. (c) The turbulent velocity field. Start time: 6 March 1997 19:35:09.

3.3.3 Air Content

The quantity of air in the water can be described in two ways. The bubble size distribution, usually represented as $n(a)da$, is the number of bubbles per unit volume, $n(a)$, in the radius range $[a, a + da]$, where the radius increment, da , is generally assumed to be one micrometre. The contribution of each radius range to the total volume of air is found by scaling the number of bubbles by the corresponding volume,

$$V_T(a) = \frac{4}{3}\pi a^3 n(a) da. \quad (3.6)$$

The total quantity of air in the volume of fluid is often required, and is simply the integral over all radii of the volume-scaled bubble size distribution,

$$\beta = \frac{4}{3}\pi \int a^3 n(a) da. \quad (3.7)$$

Because $n(a)$ is the number per unit volume per unit radius increment, β is the ratio of the volume of air to the sample volume, and is therefore known as the *air fraction*.²

Within the surf zone, bubbles range in size from the background bubbles of order 10 μm to those of order 10 mm existing immediately following a breaking event. Instruments for measuring bubble size distributions are generally capable of detecting a limited range in radii, and are further limited to a particular air fraction range. For instance, at very high air fractions, instruments using acoustical techniques tend to saturate as limitations in the electronics are reached [Vagle and Farmer, 1998]. Photographic techniques will also misrepresent the true bubble size distribution when large bubbles block small bubbles from view [Stokes and Deane, 1999]. Consequently, the use of more than one technique is desirable, and for this study, data collected by the resonator were analyzed in conjunction with data obtained by a conductivity sensor. An in-depth comparison of several bubble size measurement techniques can be found in Vagle and Farmer [1998].

An acoustical resonator mounted on the surf frame was used to measure bubble size distributions. Built at IOS, the resonator is a modification of the design developed

²In the literature, the air fraction is sometimes referred to as the void fraction.

by *Medwin and Breitz* [1989]. As its name suggests, the acoustical resonator uses both an acoustical field and resonant interactions to detect the bubble field. Knowledge of the acoustical properties of bubbles is required in order to understand how the resonator operates.

A bubble of a given radius has many modes of oscillation, the simplest being a radial expansion and contraction about the equilibrium volume. Like simple harmonic oscillators, bubbles pulsate at a natural frequency. When the surface tension and heat conduction are negligible, the resonant frequency is given by

$$f_R(a) = \frac{1}{2\pi a} \left(\frac{3\Gamma P}{\rho} \right)^{1/2}, \quad (3.8)$$

where $\Gamma = c_p/c_v$ is the ratio of the specific heats of the gas within the bubble, and P is the hydrostatic pressure. The resonant frequency therefore has a dependence not only on the bubble radius, but also on the depth at which it is located. When an acoustic pulse at the natural frequency is applied, the bubble's response is like that of a damped, forced linear oscillator [*Leighton*, 1994].

A bubble can be very effective at subtracting energy from the acoustic wave field: when at the resonant frequency, the extinction cross-section, which characterizes the amount of energy a bubble can extract from an incident wave field, is several orders of magnitude greater than the geometric cross-section! Some of the energy absorbed by the bubble is isotropically re-radiated in the form of new acoustic waves, while the remainder is lost to thermal and viscous damping.

The acoustical resonator consists of two identical circular discs, one acting as a transducer, the other as a hydrophone. In the absence of bubbles, a broadband acoustical field generated by the transducer will set up many resonant modes in the intervening volume. Bubbles that exist in the water will extract energy at their natural frequencies, thereby attenuating the resonant peaks detected by the instrument. Inverse methods are used to relate the attenuation at each resonant frequency to the number of bubbles at the corresponding radius. Further details of the instrument and the inverse methods can be found in *Farmer et al.* [1998].

Due to frequent wave breaking, the air content within the surf zone is generally quite high. Particularly during low tide, the air fraction is frequently greater than 10^{-4} , the level at which the resonator saturates. At air fractions greater than 10^{-4} , the bulk conductivity method may be used.

The conductivity of a bubble-water mixture, σ_e , is much less than that of bubble-free water, σ_0 . An estimate of the air fraction can be obtained by comparing the measured conductivity to the conductivity of bubble-free water. For air fractions less than 0.6,

$$\beta = \frac{3 - \sqrt{9 - 8\eta^2}}{2\eta}, \quad (3.9)$$

where $\eta \equiv 1 - \frac{\sigma_e}{\sigma_0}$ [Ninnis, 1991].

The conductivity of water has a strong dependence on temperature, and a lesser dependence on salinity [Lamarre and Melville, 1992]. A thermistor was installed near the conductivity cell on the surf frame, and salinity was measured by the CTD at the end of the pier. Since the near shore region is well mixed, the salinity measurements provide a good background mean level, although local fluctuations remain unknown.

The resonator is suitable for measuring air fractions ranging from 10^{-8} to $\sim 10^{-4}$, whereas the conductivity sensor provides good results for air fractions greater than 10^{-4} . The two sensors should therefore overlap for air fractions in the range from 10^{-4} to 5×10^{-4} , and for a nice example of this overlap, refer to Figure 8 in Vagle and Farmer [1998]. In practice, the unknown fluctuations in salinity introduce sufficient error in the conductivity measurements at low air fraction that this clean overlap is not generally observed. As the amount of air in the water increases, the effects of the water temperature and salinity decrease, and the conductivity sensor yields good results at the upper end of the overlap range [Svein Vagle, personal communication, 2000]. For air fractions greater than 10^{-4} , the resonator data was replaced by the conductivity data. Figure 3.9 illustrates a segment of air fraction data before and after the saturated values were replaced.

The conductivity sensor measures the bulk content of air, and can only be used

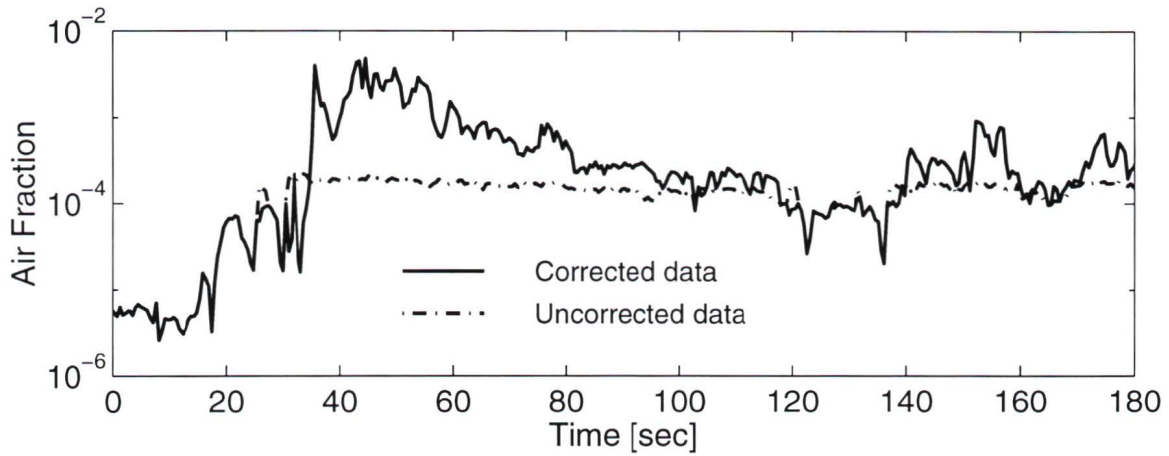


Figure 3.9: *Air fraction before and after the saturated resonator data were replaced by the conductivity data. Start time: 8 March 1997 10:01.*

to replace the resonator air fraction data. When the resonator saturates, the bubble size distribution is meaningless, and such data were therefore flagged so as not to be used in the later analysis.

4 Results

4.1 Sea State

The heights of the incoming waves are continually changing in response to the presence and duration of offshore storms. Larger waves break farther offshore, thereby changing the location and width of the surf zone. Greater incident energy is associated with larger waves, making it essential to sort the data according to sea state.

The hourly significant wave heights obtained at the seaward end of the pier have been divided into four categories, as illustrated in Figure 4.1. The difference between the extreme significant wave heights is approximately one metre. The significant wave heights illustrated in Figure 4.1 were found to be typical, spanning nearly the full range of $0.2 - 1.4\text{ m}$ observed during the entire month of March.

4.2 Wave Energy Flux

As a deep water wave approaches the shore and proceeds into water of increasingly shallower depth, interactions with the sea floor result in a wave height that increases, and a wave length and velocity that decrease such that the period remains constant [*Komar*, 1998].

Recall from equation (2.16) that the energy density is proportional to the mean

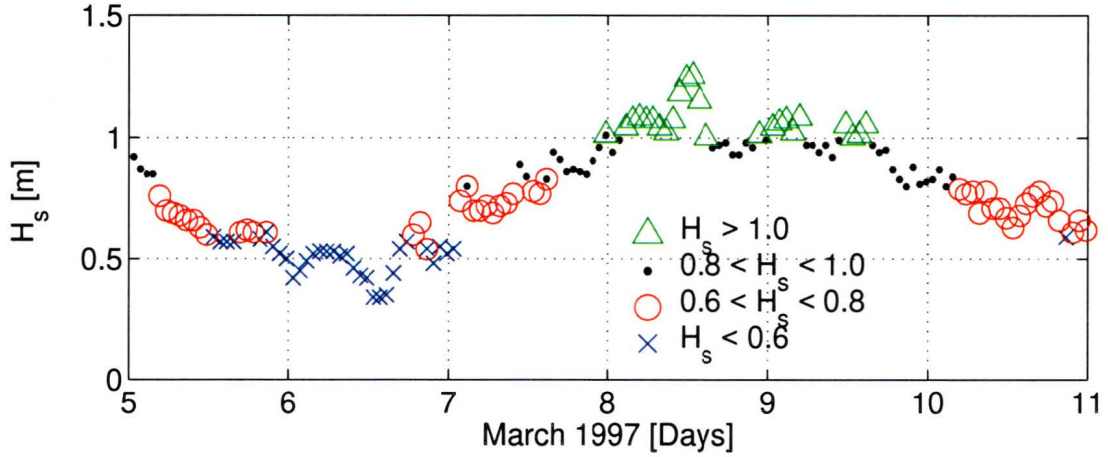


Figure 4.1: Hourly significant wave heights, H_s [m], measured at the seaward end of the pier.

square surface elevation, which, for a pure sinusoid, is given by

$$E = \frac{1}{8} \rho g H^2. \quad [J m^{-2}] \quad (4.1)$$

As a wave shoals, the wave height H increases, and by equation (4.1), the energy density is not conserved. *Kamphuis* [1991] determined from a sandy beach laboratory experiment that the energy lost to bottom friction and to percolation through the sand was negligible, so prior to breaking, there should exist neither a source, nor a sink, of wave energy. Until the wave begins to break, it is the rate at which energy is transmitted [*Komar*, 1998], or the energy flux,

$$F = \frac{1}{\rho} (E_{tot} c_g), \quad [W kg^{-1} m^2] \quad (4.2)$$

that is the conserved quantity.

A wave begins to lose energy at the onset of breaking, and continues to do so as it transforms into a propagating bore. No longer conserved, the energy flux into a given volume will be larger than the flux out [*Fredsøe and Deigaard*, 1992], and the rate of energy dissipation, integrated over the water column, is given by

$$\int_{-h}^0 \varepsilon dz = -\frac{dF}{dx}. \quad [W kg^{-1} m] \quad (4.3)$$

The dissipation rate determined from the gradient of the wave energy flux is a useful quantity to calculate as it provides an upper bound on the rate of turbulent energy dissipation. It predicts the actual dissipation rate only when turbulence is the sole sink of wave energy.

In chapter 2, the kinetic energy of a sinusoid was found to equal the potential energy. This is verified in Figure 4.2, where the kinetic energy computed from equation (2.14) is compared with the potential energy, computed from (2.15). In each of the four different wave trains analyzed (a monochromatic sinusoid, and three segments of real wave trains), we do in fact find $KE \approx PE$, and only in the presence of frequent breaking at low tide in the surf zone is the difference greater than 2%.

Since no assumption regarding the form of η was made in the derivation of the potential energy, the energy flux will be calculated using

$$E_{tot} = 2 \times PE. \quad [J m^{-2}] \quad (4.4)$$

The energy flux is illustrated in Figure 4.3. Each point represents an average over 30 minutes. At the seaward edge of the surf zone, near $x = -50 m$, the energy flux measurements are still distinctly separated according to sea state. Within the surf zone, $x \gtrsim -20 m$, the values at each depth are of the same order of magnitude, regardless of the incident wave field. This confirms the idea discussed by *Komar* [1998] that on mildly sloping beaches, the wave energy reaching the shoreline remains essentially constant. Larger incident waves break farther offshore, and if the water depth continuously decreases, the energy is simply dissipated over a wider surf zone. On a more steeply sloping beach, the energy flux would remain distinctly separated according to sea state until much closer to the shoreline.

An expanded view of the wave energy flux measurements within the surf zone is provided in Figure 4.4. A straight line least squares fit was used to obtain the integrated dissipation rate. The rates increase with increasing wave height.

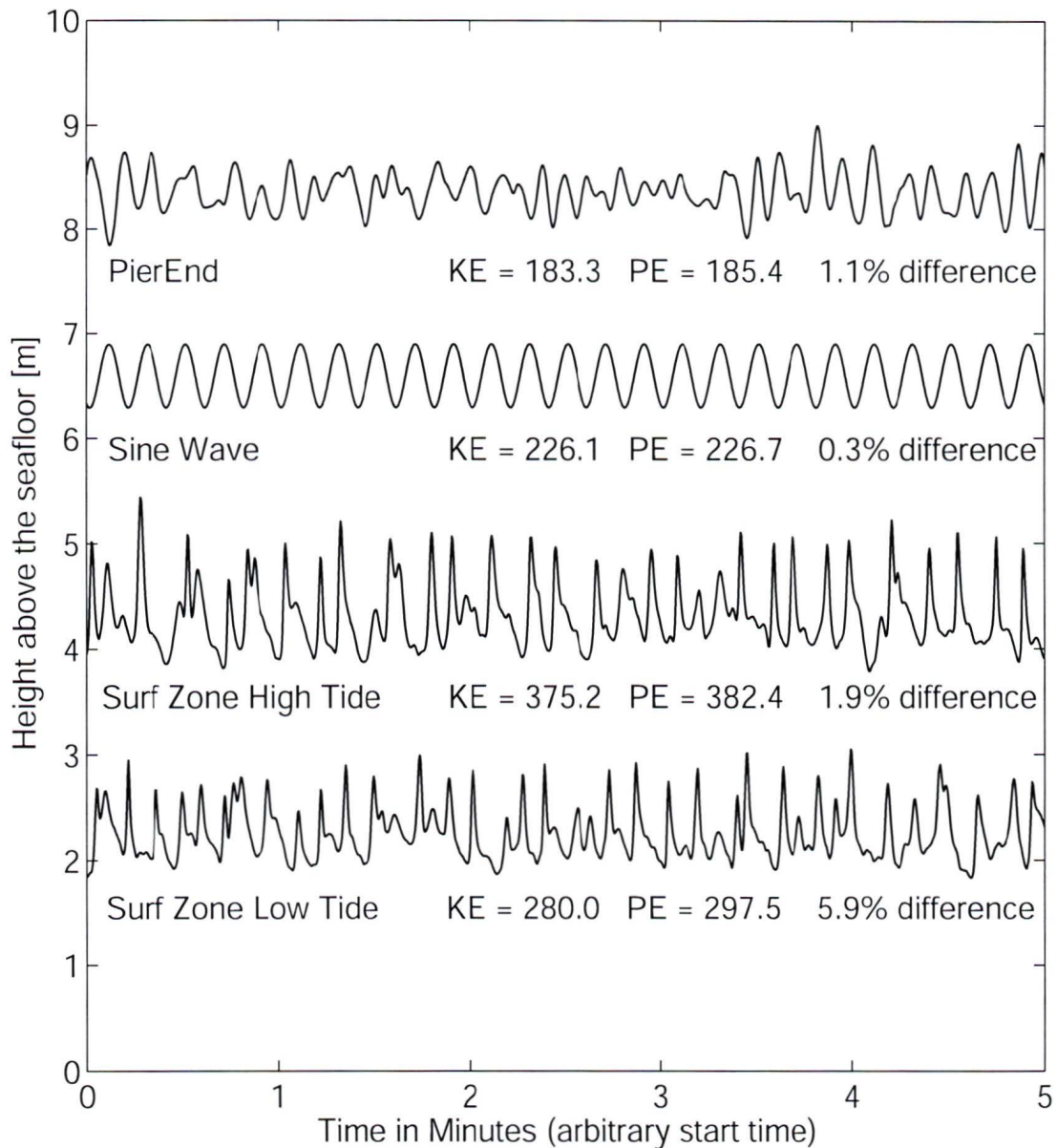


Figure 4.2: Energy calculated for various wave forms. The surf zone high tide has been displaced upward by 1.75 m for easier visibility. The sine wave was created with “typical” incoming wave values for wave height, length and period. (The unexpected difference in KE and PE in this monochromatic sine wave was introduced by the numerical nature of the computation.) Average values of KE and PE [$J m^{-2}$] were calculated over 30 minute segments; for clarity, only 5 minutes are illustrated.

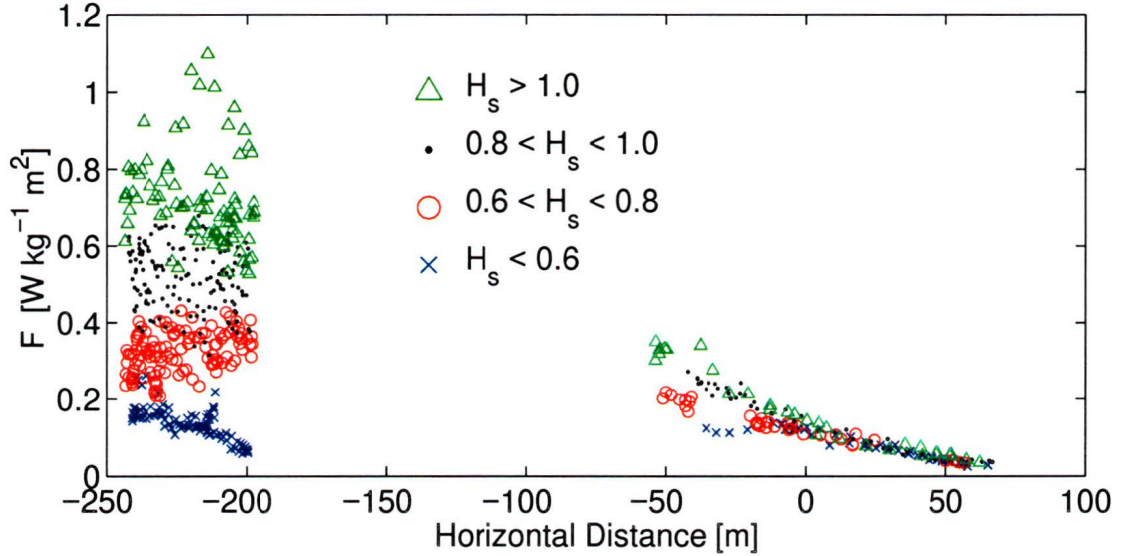


Figure 4.3: *The wave energy flux derived from 30 minute segments of sea surface elevation data. Using slopes obtained from the plot of the bathymetry, the mean water depth has been converted to horizontal distance. The origin is the location of the surf frame when in 2 m of water.*

4.3 Dissipation Measurements

Turbulence has traditionally been derived from time series measurements obtained from a single point in space. When the rms velocity fluctuations are much less than the orbital velocity, $(\overline{u'^2})^{1/2} \ll U$, and the advection time of an eddy past the instrument is much less than the characteristic eddy timescale, the turbulence will appear ‘frozen’ [Lumley and Terray, 1983]. For a steady background flow,

$$\phi(k) = \frac{\phi(f)}{2\pi/U} \quad (4.5)$$

can be used to derive the wavenumber velocity spectrum from the frequency domain.

With the ability to obtain spatial measurements nearly simultaneously, the coherent Doppler sonar provides an alternative approach to the one just described. The wavenumber spectrum can be obtained directly from each ‘snapshot’ in time. Even though the horizontal range of the sonar, R , is short compared to the wavelength,

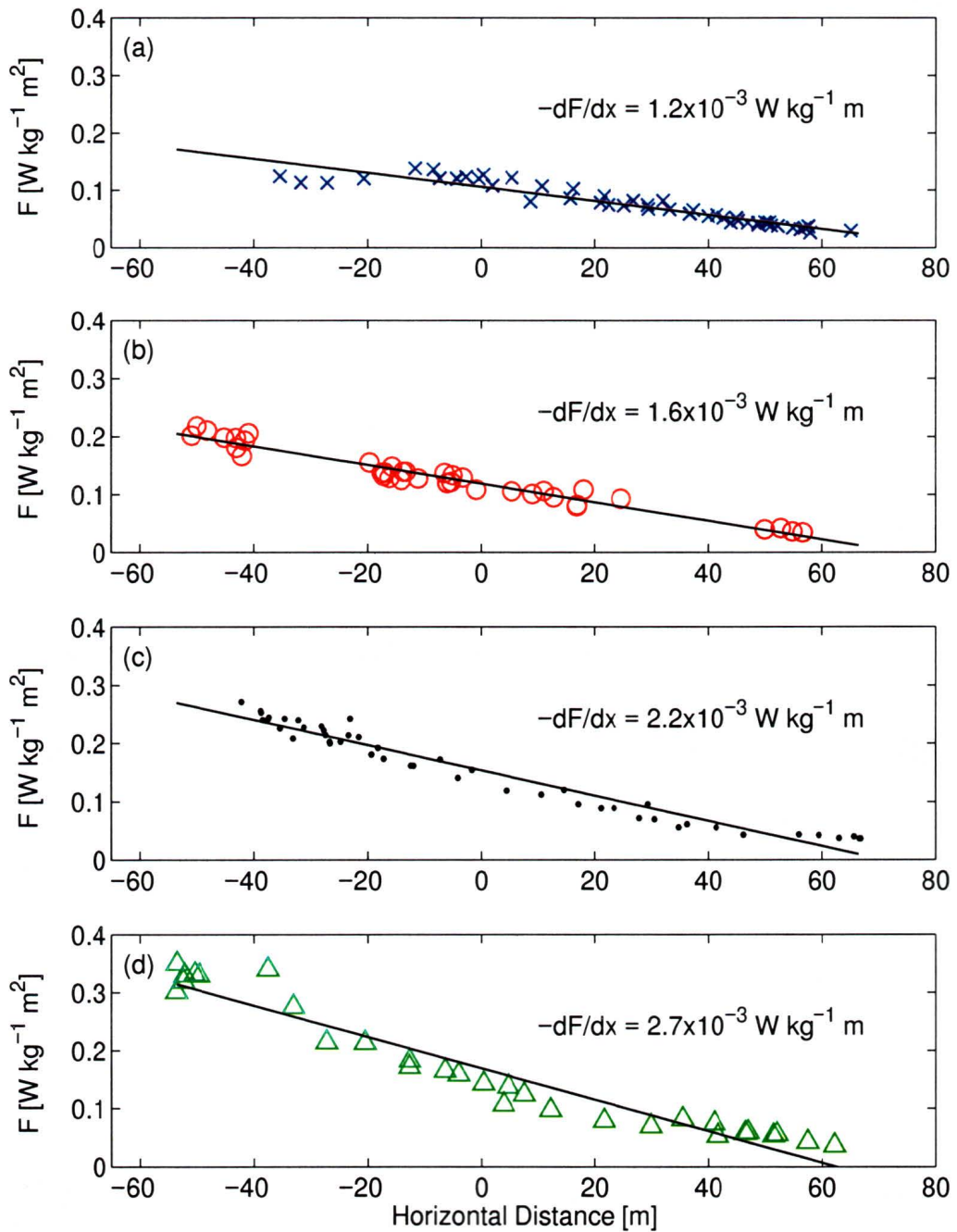


Figure 4.4: Wave energy flux within the surf zone. The symbols represent the same sea states as defined in Figure 4.1. The origin is the location of the surf frame when in 2 m of water.

$R/\lambda \sim O(1/50)$, linear trends are visible when the mean is removed, and are most pronounced in the transition regions between the peaks and the troughs in the velocity fluctuation field (Figure 4.5a). (Compare this to the velocity field in Figure 3.8c where, during the same time interval, the linear trends have been removed.) The effect the various detrending schemes have on the velocity spectrum are illustrated in Figure 4.5b. To avoid the risk of removing larger scale eddies, a lower order detrending scheme is desirable. Based on the small R/λ estimate, the linear detrending scheme should be adequate for removing the irrotational motions. As will be shown, the inertial subrange is not expected to extend to the lowest measured wavenumber, so the choice of detrending scheme is not that critical.

At high wavenumbers, the spectrum flattens out. If this is noise, then simply averaging several successive velocity measurements should reduce the noise level. Since the goal is to reduce the random noise without affecting the eddies, a limit on the number of successive records that can be averaged together is imposed by the time scale of the energy transfer through the inertial subrange, and by the time scale of particle advection across the range of the sonar. A time scale of energy transfer may be taken as $\tau \sim (k^2 \varepsilon)^{-1/3}$. Using a typical dissipation rate observed by *George et al.* [1994] of $\varepsilon = 10^{-2} W kg^{-1} m$, and $k \sim 2\pi \times 10 rad/m$ (which will be shown to fall within the inertial subrange), a time scale associated with the energy transfer is $\tau \sim 0.3 s$. This is less than or equal to the advection time scale of particles across the sonar path, in either orientation. With a sampling interval of $1/25 s$, the eddies should remain correlated between successive records if no more than 8 records are averaged together.

Figure 4.6 illustrates the two effects averaging has on the spectra. As expected, the noise level is reduced most noticeably at high wavenumbers, which changes the slope of the middle section of the spectrum. However, the level of the spectrum is also reduced at low wavenumbers. At high wavenumbers, the noise level decreases by $4 \times 10^{-6} m^2 s^2 cpm^{-1}$ after averaging over 5 records. Averaging over a further 5 records

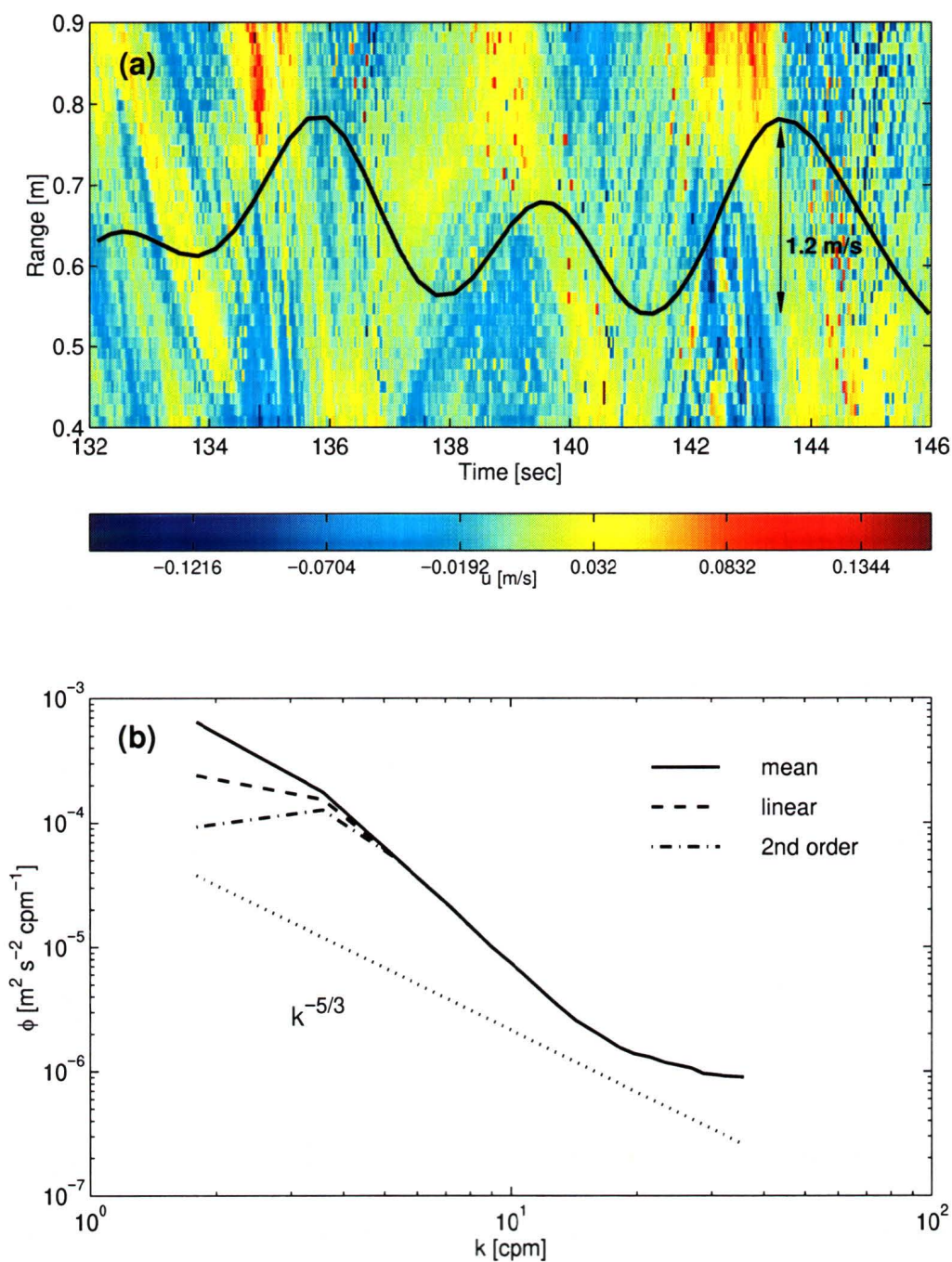


Figure 4.5: (a) Turbulent velocity field obtained by removing the mean at each time. The sinusoid is the velocity derived from the surface elevation. Start time: 6 March 1997 19:35:09. (b) The velocity spectrum for different spatial detrending schemes.

only reduces the noise level by an additional $5 \times 10^{-7} \text{ m}^2 \text{ s}^2 \text{ cpm}^{-1}$. As the spectral slope does not undergo any further significant changes, averaging over 5 records seems to provide the best balance between reducing the noise without changing the level of the spectrum too much. An average over 5 records results in a final sampling period of 0.2 s.

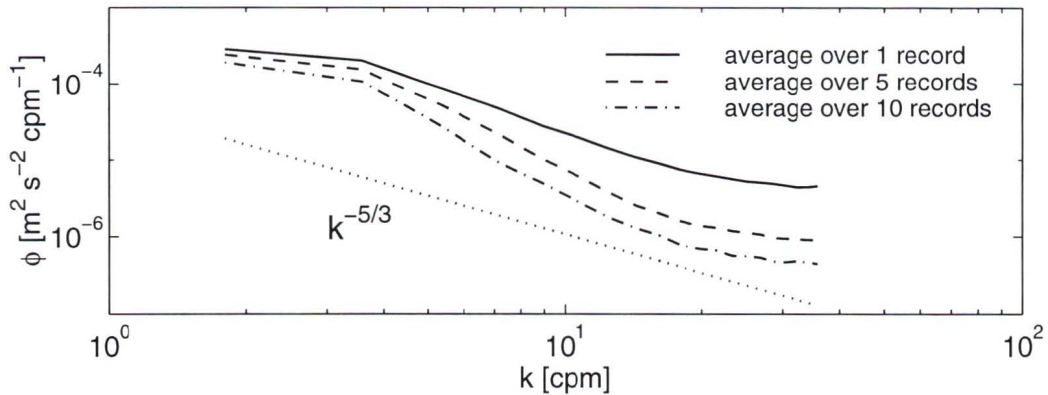


Figure 4.6: *The effect of averaging on the velocity spectrum. The sampling interval of the raw data was 0.04s. After averaging over 5 records, it is 0.2 s; after averaging over 10 records, it is 0.4 s. Data file: 03061935.*

The noise level also has a small dependence on the environmental conditions: the noise level increases slightly as the air fraction increases (Figure 4.7). Since air entrainment is associated with breaking waves, noise is therefore likely to increase with increasing levels of turbulence.

Recall from Section 2.3 that if an inertial subrange exists, the dissipation rate can be obtained from the spectrum in the wavenumber range $l^{-1} \ll k \ll \eta^{-1}$. The scale at the lower end of the wavenumber range is determined by the largest eddies. According to *Svendsen* [1987], l is only a fraction of the water depth, $l \sim 0.2h - 0.3h$. *George et al.* [1994] used $l \sim 0.25h$ in their analysis. With a mean water depth at the surf frame on the order of 2 m, $l \sim 0.5 \text{ m}$ for this study.

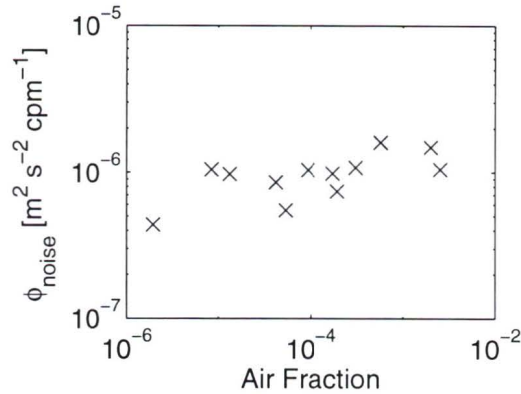


Figure 4.7: The noise level of the velocity spectra as a function of the fraction of air in the water, β .

From section 2.3, an estimate for the dissipation rate can be obtained from

$$\varepsilon \sim \frac{u'^3}{l}, \quad (4.6)$$

where u' is a typical scale for the turbulent velocity fluctuations. Inserting (4.6) into the Kolmogorov microscale (2.23), the largest expected wavenumber can then be estimated from

$$\eta = \left(\frac{\nu^3 l}{u'^3} \right)^{1/4}. \quad (4.7)$$

Taking $\nu = 10^{-6} \text{ m}^2/\text{s}$ as a typical oceanic value of the eddy viscosity, and $u' \sim 0.05 \text{ m/s}$,

$$\eta \sim 2.5 \times 10^{-4} \text{ m}. \quad (4.8)$$

The inertial subrange is therefore expected to appear in the wavenumber range $2 \text{ cpm} \ll k \ll 4000 \text{ cpm}$.

As illustrated in Figure 4.5b, the spectra were measured over the range $1 \text{ cpm} < k < 40 \text{ cpm}$. Although the lowest wavenumbers are not expected to fall within an inertial subrange, according to theory, all higher wavenumbers should. From observations in the natural surf zone, Tim Stanton found the existence of an inertial subrange at centimetre scales [*personal communication*, 2000]. However, for $k \gtrsim$

20 cpm , noise dominates. The dissipation rates will therefore be calculated from spectral values in the range

$$4 \text{ cpm} \leq k \leq 20 \text{ cpm}, \quad (4.9)$$

which corresponds to length scales of 5 – 25 cm .

The nature of the turbulence is expected to depend on the location within the nearshore region. Although waves are repeatedly breaking in the surf zone, breaking at any fixed point in space is unsteady. High intensity turbulence will therefore be intermittent, and it is likely to be dominated by the effects of strong shear and buoyancy. Seaward of the main breaker zone, turbulence diffuses upward from the bottom boundary, and in the presence of a rip current, may also be advected from farther inshore. Strong shear and large air fractions are less likely to occur, and the turbulence is expected to be more steady, and of lower intensity.

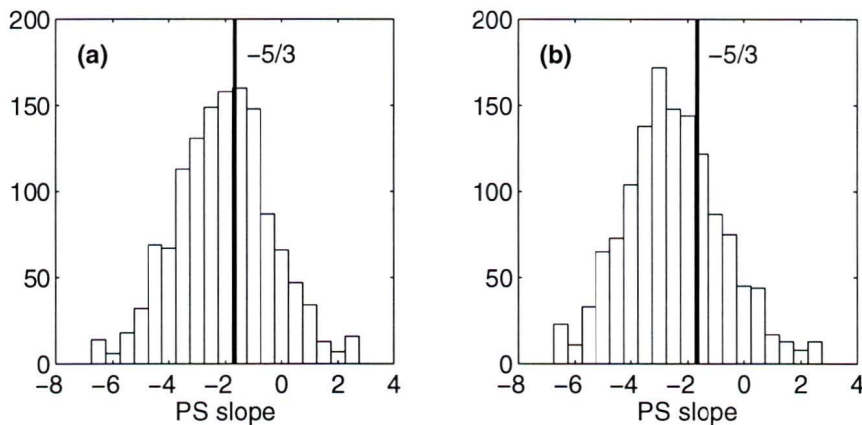


Figure 4.8: Histograms of the spectral slopes from 5 minute data segments. (a) High tide when there were few breaking waves (10 March 10:24). (b) Low tide in the presence of frequent breaking (8 March 10:00).

Some evidence of this difference can be found in the spectral slopes, which are computed by a least squares fit in the inertial subrange. Figures 4.8a and 4.8b illustrate histograms of spectral slopes at high and low tide, respectively. Outside the surf zone, the spectral slope tends to $-5/3$, whereas in the presence of frequent breaking,

the slopes tend to be more steep. Application of Kolmogorov's theory to compute the dissipation rate requires a spectral slope of $-5/3$ within the inertial subrange. However, when interpreting the data, it is important to keep in mind that this is a necessary, but not sufficient, condition of the Kolmogorov theory.

In chapter 2, it was found that the velocity spectrum could be written in terms of the dissipation rate. Inverting equation (2.21), the dissipation rate is given by

$$\varepsilon(k) = \left(\frac{55}{27}\right)^{3/2} \phi^{3/2} k^{5/2}. \quad [W kg^{-1}] \quad (4.10)$$

If an inertial subrange exists, ε should be independent of k over that range. The sample illustrated in Figure 4.9 indicates there is some variability, so the dissipation rate is taken as the mean, $\varepsilon = \overline{\varepsilon(k)}$. Most of the data fall within the range $1 \times 10^{-6} - 5 \times 10^{-3} W kg^{-1}$, although some rates are as low as $2 \times 10^{-8} W kg^{-1}$ and as high as $5 \times 10^{-2} W kg^{-1}$.

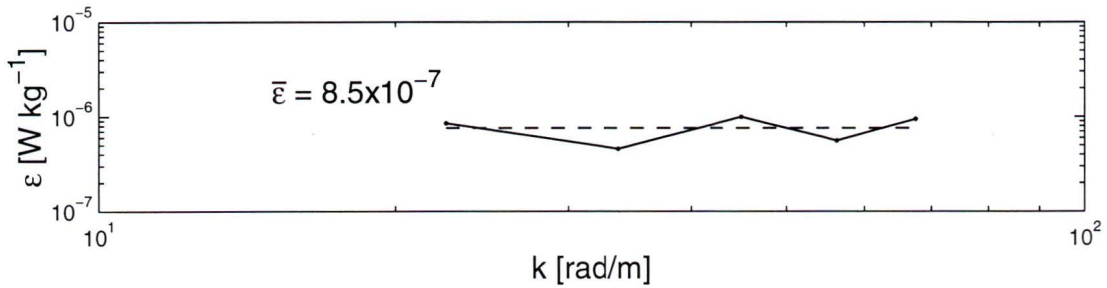


Figure 4.9: *The dissipation rate as a function of wavenumber (10 March 1997 10:24:26).*

Along with the surface elevation and air fraction, a sample time series of the dissipation rate is illustrated in Figure 4.10. Based on the slope of the front of the wave, the (Δ) indicate waves that are likely spilling breakers. (No pier video recording was available for this segment to confirm these guesses.) Examination of several other segments revealed no clear relationship between the breaking wave and the dissipation rate, although because the air fraction was not exceptionally high, this may be due to the weak nature of the breaking waves.

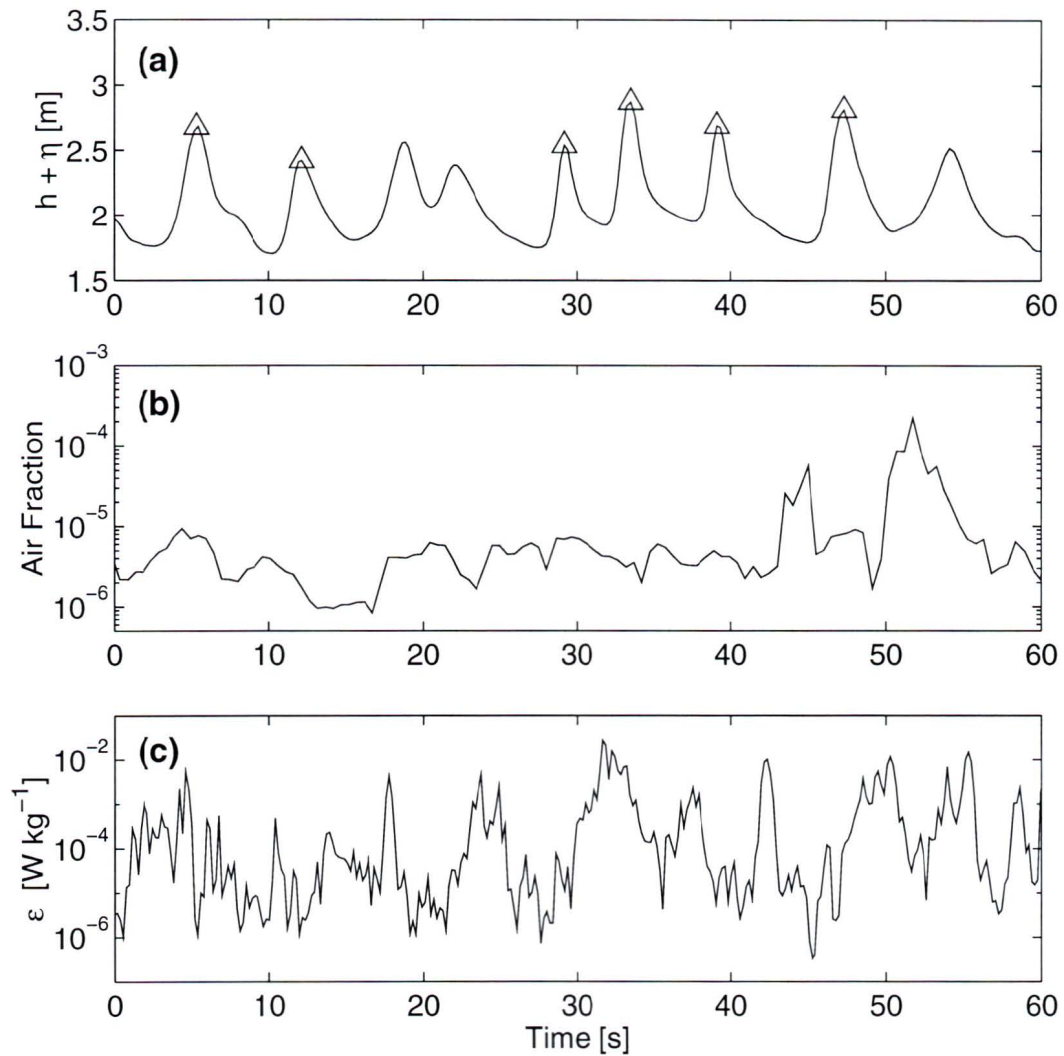


Figure 4.10: (a) The surface elevation. The (Δ) indicate waves that may be breaking (see text). (b) The air fraction. (c) The dissipation rate. Start time: 6 March 1997 21:02:55.

4.4 Bubble Evolution

Wave breaking leads to the injection of air into the water column and the subsequent formation of air bubbles, as described in Chapter 2. Figure 4.11 illustrates the jump in air fraction following a gently spilling breaker, in this case, an increase by three orders of magnitude. The fluctuations with each passing wave, an indication that the bubble cloud tracks the surface, illustrate the non-stationarity of the clouds. The fixed instrument therefore samples different vertical sections of the cloud as the water depth changes. The composition of the bubble cloud also changes, as indicated by the decrease in mean air fraction over the 40 seconds following the breaking event. Although not resolved by the fixed sensor, it is also important to consider the possible advection of the clouds by mean currents.

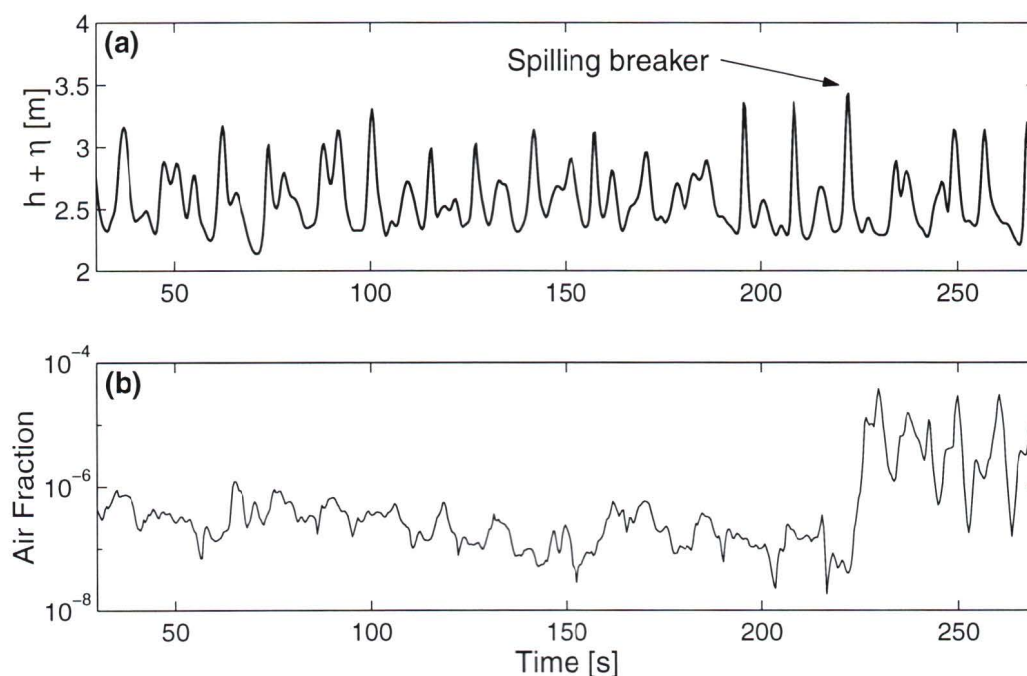


Figure 4.11: (a) Surface profile. (b) Air fraction measured at 1.5 m above the sea floor. Start time: 10 March 1997 10:24:25.

The size distribution also changes after a breaking event. Figure 4.12 illustrates

the volume-scaled size distribution prior to, and following the event indicated in Figure 4.11. The distributions are each averaged over approximately 45 seconds. Several changes are observed. As expected from the increase in air fraction, there is an increase in the volume contribution at each bubble size. The volume-scaled distribution becomes flatter following the wave breaking, and the bubble size contributing most to the air fraction shifts to a larger radius. Before breaking, the peak was near $45 \mu\text{m}$; after breaking, the peak increased to nearly $130 \mu\text{m}$. Compare these values with those in the open ocean, where at a sampling depth of 0.7 m , the shift in peak contribution was from $\sim 80 \mu\text{m}$ to $\sim 200 \mu\text{m}$ [Farmer *et al.*, 1998]. Terrill and Melville [2000] found that radii in the range $60 - 90 \mu\text{m}$ contribute most to the air fraction at $1 - 2 \text{ m}$ downstream from laboratory breaking waves.

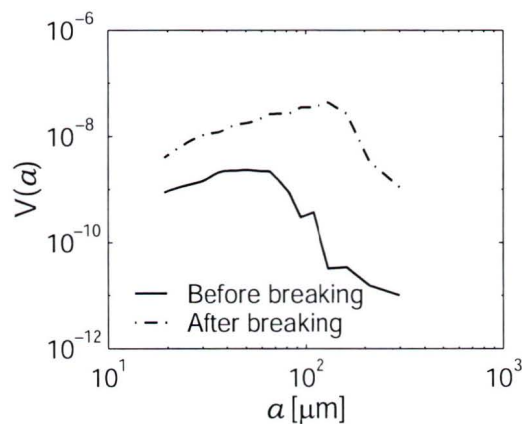


Figure 4.12: *The volume-scaled bubble size distribution averaged over approximately 45 seconds before and after the breaking event in Figure 4.11.*

The air fraction level prior to the breaking event illustrated in Figure 4.11 is assumed close to the background ambient level since there was no breaking directly over the instrument for at least 5 minutes, although some bubbles may have advected into the path of the resonator from breaking farther in-shore. This isolated breaking is a rare occurrence. From observations made at high tide from Scripps Pier, waves generally approach the beach in packets. This can be seen in the short segment

of surface wave profile at the end of the pier illustrated in Figure 4.2. Within any particular packet, consecutive waves generally break, followed by up to several minutes without breaking. There are few waves from which the evolution of the bubbles can be examined without being affected by subsequent injection events.

How does the bubble size distribution evolve immediately following a breaking event? The time series illustrated in Figure 4.13 was chosen because of the lull in breaking that allows an analysis of the decay of bubbles from a single event over approximately 60 seconds. Some caution must be taken with this analysis as the advection of the bubble cloud may introduce variations that cannot be removed. Figure 4.13a illustrates the surface wave profile. Figure 4.13b illustrates the air fraction, with the numbers indicating the times at which the volume-scaled size distributions in Figure 4.14 were extracted. (For comparison, the dissipation rates measured in the surf zone were also included in Figure 4.13c, but discussion of turbulence will be left until the next chapter.) Several main features are observed in the size distributions in Figure 4.14. First, the volume contribution decays with each successive profile, supporting the view that no breaking occurred between 65-105 seconds. It also suggests that bubbles are continually being lost at the surface. Second, within 40 seconds, the peak shifts from $100 \mu m$ to $60 \mu m$. Finally, the number of small bubbles fluctuates, possibly being an indicator of larger bubbles dissolving into smaller bubbles.

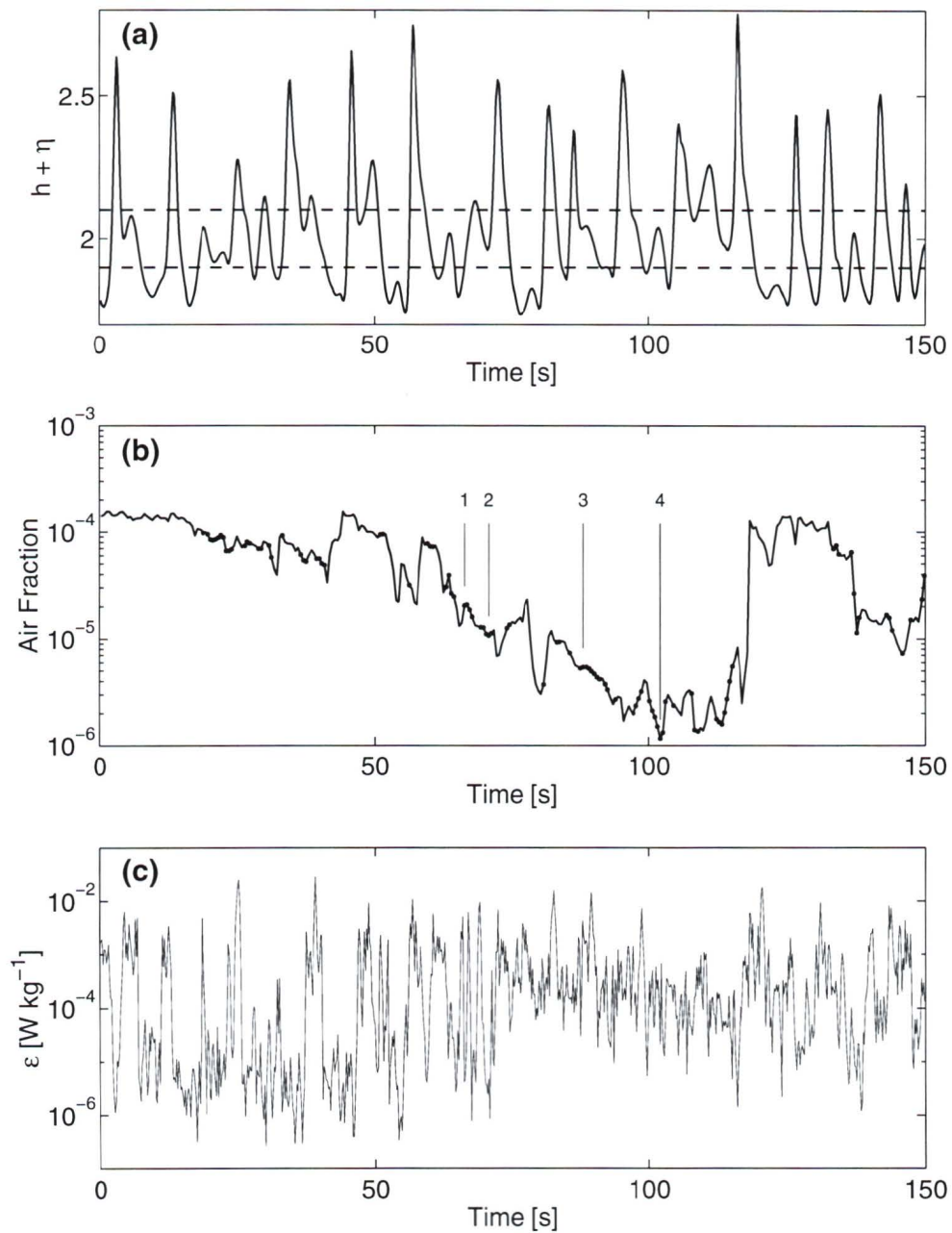


Figure 4.13: (a) The surface elevation. (b) The air fraction; the numbers represent the times at which the volume-scaled bubble size distributions illustrated in Figure 4.14 were extracted. (c) The dissipation rate. Start time: 5 March 1997 20:04:00.

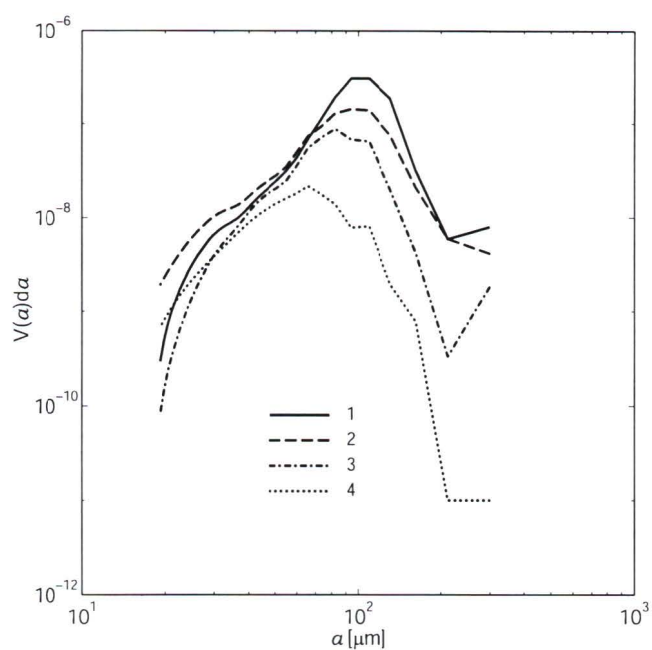


Figure 4.14: *Volume-scaled bubble size distributions extracted at the times indicated by the numbers in Figure 4.13b. The size distributions were extracted only when the instrument was between 0.35 – 0.55 m beneath the (level) surface.*

5 Discussion

5.1 Energy Considerations

In the previous chapter, energy dissipation rates integrated over the water column were calculated from the change in wave energy flux. Since it is unlikely that the energy is dissipated uniformly over the entire water depth, the significant wave height will be used as a normalizing length scale. The normalized wave energy dissipation rates can then be compared with the rates derived from the turbulent velocity fluctuations (which were not integrated over the water depth). As illustrated in Figure 5.1, the mean turbulent energy dissipation rate measured at 1.75 *m* above the sea floor is always less than the mean wave energy dissipation rate. This was expected, as the wave energy dissipation rate provides a maximum bound on the rate at which the energy is dissipated.

It is interesting to note a few features of the rates illustrated in Figure 5.1. Although the integrated wave energy dissipation rate increases with increasing sea state (Figure 4.4), since a larger gradient in the wave energy flux corresponds to a larger incident wave field, the normalized rates are all approximately $\frac{-1}{H_s} dF/dx \sim 2 \times 10^{-3} W kg^{-1}$. The measured dissipation rates show no dependence on the sea state either. The only visible trend in the measured rates is a slight decrease with increasing water depth. In the deeper water, the instrument is both farther from the

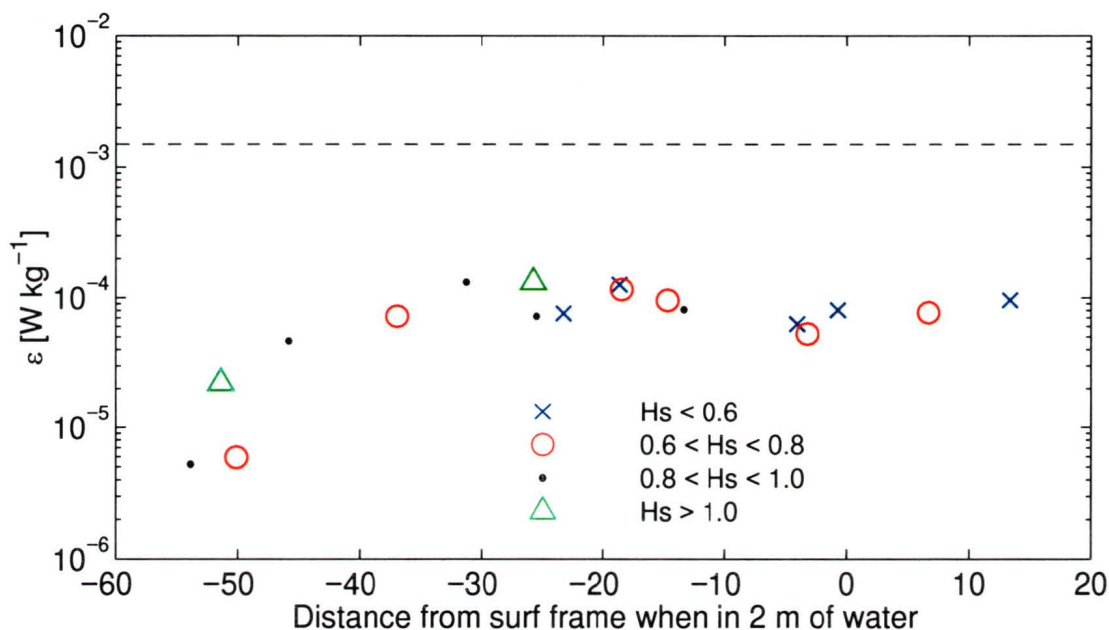


Figure 5.1: Comparing the mean wave energy dissipation rate (dashed line) to the mean measured turbulent dissipation rates (symbols). The symbols represent the different sea states originally defined in Figure 4.1.

surface and farther off-shore from the main breaker line, where fewer breakers pass directly over the instrument. Since the dissipation rate decreases with decreasing frequency of breaking, it is likely that breaking waves are the primary source of energy at the height of the instrument. In contrast, as the water depth decreases and the frequency of breaking increases, the measured dissipation rates tend to level off, suggesting some manner of saturation is reached. This saturation may be physical, or it may be a limitation imposed by the instrument.

Since the energy dissipation rates measured within the water column are less than the maximum determined by the changing wave heights, the energy must either be dissipated elsewhere in the water column or by other mechanisms. Several investigators, including *Svendsen* [1987] and *Ting and Kirby* [1996], have suggested that most of the energy in a spilling breaker is dissipated above trough level. If dissipation due to bubble injection and as a result of bottom friction is found to be small compared

to the available energy, then it is likely that most of the energy is indeed dissipated in the near-surface layer above the instrument.

5.1.1 Energy Loss through Bubble Entrainment

The entrainment of air is a sink of wave energy because work is required to overcome the buoyancy force of the bubbles. Since the bubbles eventually rise to the surface, this change to potential energy is only temporary. Some of the energy may be transferred into turbulent kinetic energy by the wakes generated by the rising of the bubbles.

The increase in potential energy associated with the entrainment of air is calculated from the difference in potential energy before and after mixing. Consider a thin surface layer of air of thickness Δd and density ρ_{air} , overlying a layer of bubble-free water of thickness $d - \Delta d$ and density ρ . After mixing, the bubbly water will occupy the full mixed layer d , and using the conservation of mass, will have a density of $\rho' = \rho - (\rho - \rho_{air}) \frac{\Delta d}{d}$. The change in potential energy associated with the mixing is given by

$$\begin{aligned} \Delta PE &= \rho' g \int_{-d}^0 z dz - \left(\rho g \int_{-d}^{-\Delta d} z dz + \rho_{air} g \int_{-\Delta d}^0 z dz \right) \\ &= \frac{1}{2} g \left[(\rho - \rho_{air}) \Delta d d - (\rho - \rho_{air}) \Delta d^2 \right]. \end{aligned} \quad (5.1)$$

Taking Δd to be small, since $\Delta d \ll d$, the last term is negligible. Furthermore, since $\rho_{air} \ll \rho$, equation (5.1) simplifies to $\Delta PE = \frac{1}{2} \rho g \left(\frac{\Delta d}{d} \right) d^2$. Recalling the definition of the air fraction, for any given surface area, $\beta \equiv \frac{V_{air}}{V_{total}} = \frac{\Delta d}{d}$, and the change in potential energy can be further simplified to $\Delta PE = \frac{1}{2} \rho g \beta d^2$.

The rate of creation of potential energy over a wave period is equivalent to the rate of loss of wave energy, and is given by

$$B \equiv \frac{\Delta PE/T}{\rho} = \frac{1}{T} \frac{1}{2} g \beta d^2, \quad [Wkg^{-1}m] \quad (5.2)$$

where T is the wave period. Immediately following a breaking event, the air fraction above the wave trough is very high, with $\beta \sim O(10^{-2})$ [Deane and Stokes, 1999].

Taking $d = 0.5 m$ to be a typical wave height, and a mean wave period of $T \sim 10 s$, the rate of creation of potential energy is $B \sim 1.3 \times 10^{-3} W kg^{-1} m$. This value is on the same order of magnitude as the rate of dissipation of the wave energy.

Since the large bubbles rise rapidly to the surface, air fractions of this magnitude are rarely observed at the depth of the instrument, and are furthermore unlikely to be observed deeper in the water column. Taking $\beta \sim 10^{-4}$ as being more representative of the air fraction throughout the entire depth $d \sim 2 m$, $B \sim 2 \times 10^{-4} W kg^{-1} m$. The bubbles that are entrained to the depth of the instrument are therefore unlikely to be the dominant sink of energy in a breaking wave. However, the energy required for the initial entrainment of air in the region of high bubble density above the wave trough is significant.

5.1.2 Energy Loss at the Bottom Boundary

Earlier calculations of wave energy flux involved the assumption that energy was not dissipated prior to breaking. However, since percolation through sand, friction at the boundary, and movement of the sea bed are all energy sinks, there is likely to be at least a small loss at the sea floor. *Shemdin et al.* [1978] found that at the bottom boundary, the dominant sink of wave energy is dependent on the characteristics of the sea floor: percolation dominates when the sea floor is composed of a coarse sand (mean diameter $> 0.5 mm$); bottom friction dominates when the sand grains are fine (mean diameter $< 0.4 mm$); and bottom motion dominates when the sea bed is composed of silt, clay, or soft organic matter. According to *Deane* [1997], the beach near Scripps Pier is composed of a fine grain sand, with a mean particle diameter in the range $0.2 - 0.5 mm$, so friction is expected to be the dominant energy dissipation mechanism near the bottom boundary.

As a result of the interest in sediment transport, the interactions of waves and currents with the sea bed have been well studied, particularly by coastal engineers. According to *Sarpkaya and Isaacson* [1981], the average rate of dissipation for an

oscillatory flow is

$$D = \overline{\tau u}, \quad (5.3)$$

where τ is the shear stress at the bottom, u is the velocity at the outer edge of the boundary layer, and the overbar denotes a temporal average. In the literature [Jonsson, 1966; Grant and Madsen, 1979; Christoffersen and Jonsson, 1985], the shear stress is commonly defined in terms of a coefficient of friction, f , as

$$\tau = \frac{1}{2} f u^2. \quad (5.4)$$

Letting $u = u_0 \cos \omega t$, we find that

$$D = \frac{2}{3\pi} f u_0^3. \quad [Wkg^{-1}m] \quad (5.5)$$

For a boundary layer of thickness δ , where $\delta \ll h$, the velocity developed by linear theory is

$$u_0 = u(\delta - h) = \frac{H}{2} \omega \frac{1}{\sinh kh}. \quad (5.6)$$

Typical values of the wave parameters in the surf zone are as follows: $T = 6$ s; $\lambda = 35$ m; $H = 0.5$ m; and $h = 2$ m. The velocity just above the boundary layer is then found to be $u_0 \sim 0.6$ m/s.

Determination of the friction factor is less straight forward, and is generally determined from laboratory studies [Jonsson, 1966]. The following empirical relation is suggested by Fredsøe and Deigaard [1992]:

$$f = 0.04 \left(\frac{a_\delta}{k_N} \right)^{-1/4}, \quad (5.7)$$

where a_δ is the maximum horizontal amplitude of the motion just above the boundary layer, and k_N is the Nikuradse bottom roughness. Using linear theory and $\delta \ll h$, the amplitude of horizontal displacement of a particle at depth $\delta - h$ is given by

$$a_\delta = \frac{H}{2} \frac{1}{\sinh kh}. \quad (5.8)$$

Using the same typical values for the parameters as before, $a_\delta \approx 0.6$ m.

The effect of the bottom boundary is parameterized by the Nikuradse bottom roughness, k_N , which has units of length. *Shemdin et al.* [1978] found that with a continuous covering of ripples on the sea floor, k_N was on the order of the ripple height, whereas in the absence of a steady covering of ripples, k_N was on the order of the sand grain diameter. At the beach near Scripps Pier, ripples are present outside the surf zone, but within the breaker zone, ripples make up only a very sparse covering [*Dale Stokes*, 2000, *personal communication*]. Choosing an intermediate bottom roughness of $k_N = 0.01\text{ m}$, the coefficient of friction is found to be $f \sim 10^{-2}$. So $D \sim 4 \times 10^{-4}\text{ Wkg}^{-1}\text{ m}$, and

$$\frac{D}{-dF/dx} \sim 2 \times 10^{-1}. \quad (5.9)$$

The energy dissipated at the bottom boundary is much less than the total energy dissipated by the wave.

5.1.3 Turbulent Kinetic Energy in the Water Column

The previous calculation compared the wave energy dissipation to the bottom boundary dissipation. What follows will examine the eddy viscosity, an indirect comparison of the observed turbulent kinetic energy to that generated by the interactions of the currents and the wave orbital motion with the sea floor. *Christoffersen and Jonsson* [1985] developed a generalized model with variable current speed and direction to predict the eddy viscosity field. *Vagle et al.* [in press, 2000] used the *Christoffersen and Jonsson* [1985] model to study bubbles carried seaward by rip currents, and a modification of this implementation is used in the following.

In addition to the water depth, the model requires input parameterization of the waves, the current, and the bottom boundary. The current is parameterized by the speed, U , and the direction, ϕ , taken with respect to the cross-shore axis. Insignificant changes were observed as ϕ was varied from 0 (cross-shore) to $\frac{\pi}{2}$ (longshore). U was varied from 0 to the maximum observed current speed of order 1.5 m/s . The waves are

parameterized by the horizontal amplitude of the wave above the bottom boundary, the mean wave period, T , and the wave angle with the cross-shore axis, θ . As before, the bottom boundary is parameterized by the Nikuradse bottom roughness, k_N .

The model, described in detail in *Christoffersen and Jonsson* [1985], used an iterative procedure to calculate the shear stress, $\boldsymbol{\tau}$. The eddy viscosity is then obtained from

$$\nu_T = \begin{cases} \kappa z \left(1 - \frac{z}{h}\right) \sqrt{\frac{\tau_c}{\rho}} & \delta < z \leq h \\ \beta k_N \sqrt{\frac{\tau_m}{\rho}} & 0 \leq z \leq \delta \end{cases}$$

where $\kappa = 0.40$ is the von Kármán constant, $\beta = 0.0747$ is a turbulence constant, τ_m is the maximum of, and τ_c is the magnitude of the steady part of, the bed shear stress. Figures 5.2a and 5.2b illustrate the theoretical eddy viscosity field for the average rip current speed and the maximum expected velocities, respectively. The dashed white lines indicate the height of the coherent Doppler sonar above the sea floor.

According to *Svendson* [1987], the eddy viscosity is related to the turbulent kinetic energy by

$$\nu_T = l\sqrt{k}, \quad (5.10)$$

where l is a turbulent length scale and $k = \frac{1}{2}(\overline{u'^2} + \overline{v'^2} + \overline{w'^2})$. The coherent Doppler sonar measured only one component of the velocity (u for the first two days; v for the remainder of the experiment). According to *Svendson* [1987], laboratory studies have found that for breaking waves, $\overline{u'^2} > \overline{w'^2}$ and $\overline{v'^2} \sim O(\overline{w'^2})$, with the exact relation being best described by that for a plane wake:

$$\left(\frac{\overline{u'^2}}{2k}, \frac{\overline{v'^2}}{2k}, \frac{\overline{w'^2}}{2k}\right) = (0.42, 0.26, 0.32). \quad (5.11)$$

Using the above relation, and following *Svendson* [1987] in choosing $l = 0.25h$ since l is length scale associated with the energy-containing eddies, the eddy viscosity for each data segment can be computed. Since the model requires a time independent

current, a steady state is being assumed. For this reason, an average eddy viscosity will be computed for each of the 5-minute data segments.

Figure 5.2c compares theory (lines) to observations (\times). The observed eddy viscosities are much greater than theory, suggesting that the turbulence generated at the bottom boundary is not a dominant sink of wave energy. Note that the one theoretical profile having the same order of magnitude as the observations was produced using gross overestimates of the input parameters. Although velocities of 1.0 m/s were recorded during the 1999 experiment, steady state currents rarely rose much above the average of 0.2 m/s . The same is expected to hold during the 1997 experiment since the sea states were similar. The roughness of 0.5 m is similarly unreasonable in this particular part of the nearshore region.

5.1.4 Discussion

The energy dissipated during the entrainment of air to the depth of the instrument and at the bottom boundary were both found to be an order of magnitude less than the total energy dissipated by the wave, suggesting that neither process is the dominant sink of wave energy.

The most realistic eddy viscosity predicted by the model (the solid line in Figure 5.2c) was much less than those derived from the measurements. More importantly, to achieve the observed values, gross overestimates of the parameters were required, indicating that a very different physical environment would be necessary before the bottom turbulence would show such large intensities. Particularly during low tide, it is unlikely that the instrument measured any significant bottom generated turbulence. The turbulence measured by the sonar must therefore be the result of surface processes.

Since the measurements account for only a small portion of the dissipated wave energy, most of the energy must be dissipated at depths shallower than the level of the sonar. Estimates of the energy dissipated during the entrainment of large

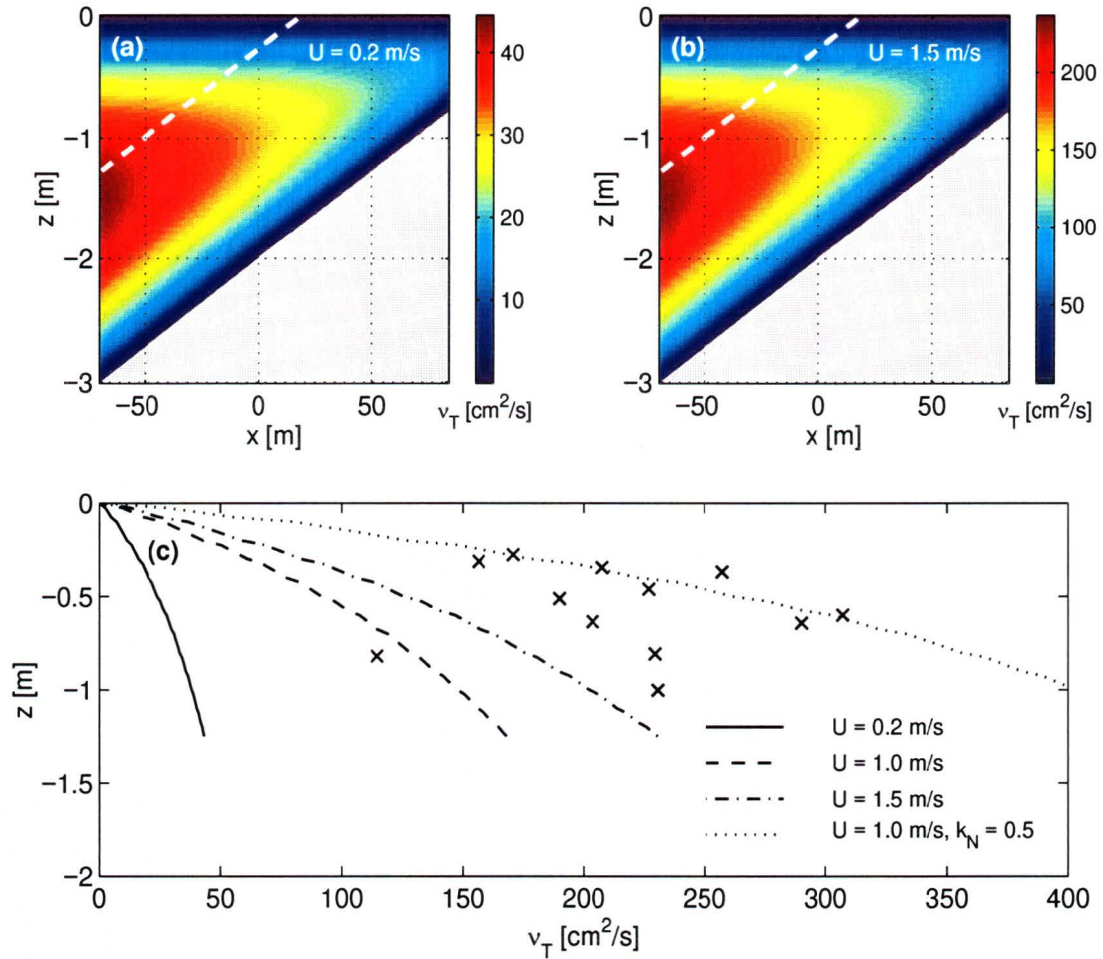


Figure 5.2: The theoretical eddy viscosity, ν_T , calculated for a current of speed (a) $U = 0.2$ m/s and (b) $U = 1.5$ m/s. The dashed white lines indicate the height of the sonar. (c) Theoretical ν_T extracted at the instrument height (lines) compared to ν_T derived from the measured turbulent velocity fluctuations (\times). Except where otherwise specified, $k_N = 0.01$. The solid line is the most likely curve, since the average background currents were unlikely to rise above 0.2 m/s

volumes of air in the region above the trough level were found to be comparable to the dissipated wave energy. This suggests that the energy dissipation is further localized to the region between the wave trough and crest. Moreover, the energy dissipated by a breaking wave is dominated by two processes: turbulence and the entrainment of air to a level above the trough.

5.2 The Generation of Persistent Bubble Clouds

5.2.1 Processes Affecting Bubble Clouds

As discussed in chapter 2, bubble clouds are created when air pockets injected into the water column by breaking waves collapse to form bubbles. If bubble injection events occur at intervals less than the time it takes for the bubbles to disappear, either by rising to the surface or through dissolution, a persistent bubble cloud is generated. An acoustical barrier inhibiting signal propagation is thereby created by these clouds, or *bubble barriers*. While of obvious relevance to the development of acoustical remote sensing in the surf zone, the presence of the quasi-steady bubble barrier provides some insight into the balance between different physical processes in the environment.

The main processes controlling the generation and persistence of the bubble barrier are the intermittency of the breaking events, bubble buoyancy and dissolution, and turbulence. The effect of the intermittency is independent of the other processes, and determines the frequency at which bubble replenishment will occur. There is a complex interplay between the remaining processes, and these will be explored in detail in the next section through a consideration of the relevant scales. First, however, the effect of each process taken in isolation will be discussed.

Buoyancy Effects. Bubbles rise buoyantly at a rate determined by the bubble size, with rise speed increasing with increasing radius (Figure 2.4). Buoyancy acts to sort the bubbles according to size.

Bubble Dissolution. Bubbles tend to dissolve at a rate dependent on the bubble size, the state of the bubble wall, and the saturation level of the water. For very high saturation levels, a bubble may even increase in size.

Turbulence. In addition to a buoyant rise, bubbles are moved passively by fluid motions. Turbulent diffusion mixes the bubbles throughout the water column and therefore acts to delay the surfacing of bubbles that are advected deeper than the initial injection depth.

The interdependence of the processes increases the complexity of the system. For instance, the bubble rise speed will decrease as the bubble dissolves. Scale analysis will be used to look at limiting cases, and this, in addition to a simple model, will be used to discuss the generation of persistent bubble barriers.

5.2.2 Scale Analysis

Turbulence-Buoyancy. In the presence of turbulence, the bubble has a vertical velocity of $w = w_b + w'$. Only when $w' \ll w_b$ is the effect of turbulence negligible, with the bubble rising to the surface as if in still water. In all other cases, the turbulence intensity is sufficiently large to have an effect on the resulting bubble motion. In the extreme case where turbulent diffusion dominates, as might occur for the smallest bubble sizes, buoyant effects are insignificant.

Turbulence-Dissolution. If turbulent diffusion dominates the bubble advection because the bubble is very small (and not because the turbulence is exceptionally strong), the bubble will dissolve long before reaching the surface.

Buoyancy-Dissolution. Dissolution effects, which can be ignored when the rise time of the bubbles is much less than the time it would take that same bubble to dissolve, are expected to be negligible for the largest bubbles, which have a large rise speed and a long dissolution time. When the two time scales are on the same order of magnitude, the processes become coupled, since the decreasing radius of the dissolving bubble will result in a decreasing rise speed and an increasing dissolution

rate. Eventually, when the bubble is small enough, the buoyancy effects may even become negligible. The bubble size at which the effects become coupled is depth-dependent since a greater injection depth will result in a longer rise time.

The generation of sustained bubble clouds requires that a sufficient number of bubbles survive from one injection event to the next. Bubbles at the extreme ends of the size spectrum are likely to disappear between events due to dissolution (at small sizes) and surfacing (at large sizes). The intensity of the turbulence, which controls the diffusion of bubbles, and the frequency of breaking will determine whether bubbles at intermediate sizes will persist.

5.2.3 A Simple Model for the Turbulent Diffusion of Bubbles

The effect turbulence has on a single bubble can be modeled as a random walk problem. For a cloud of bubbles, the distribution with time is better described by diffusion. Consider a cloud composed of bubbles of a single radius. The spatial distribution evolves from the initial delta function, centered about the injection depth, into a Gaussian distribution. The spreading cloud rises at the buoyant rise speed.

A simple model of diffusion will be used to explore the persistence of bubble clouds in turbulent water. Changes in bubble size due to dissolution and pressure effects will be ignored, although a comment on the time scale of dissolution will follow in the next section.

The model is based on the advection-diffusion equation (discussed in more detail in *Fischer et al.* [1979]),

$$\frac{\partial N}{\partial t} + w_b \frac{\partial N}{\partial z} - K_\nu \frac{\partial^2 N}{\partial z^2} = 0, \quad (5.12)$$

where N is the number density, and K_ν is the diffusion coefficient. Following *Thorpe* [1984b], we assume that the turbulent diffusion coefficient for bubbles, K_ν , is equal to that of momentum, the eddy viscosity ν_T . The solution to the problem when a

solid boundary is imposed at the bottom is

$$N(z, t) = \frac{N_0}{\sqrt{4\pi K_\nu t}} \left(e^{-[z-(z_0+w_b t)]^2/4K_\nu t} + e^{-[z-(-2h-(z_0+w_b t))]^2/4K_\nu t} \right), \quad (5.13)$$

where z_0 is the injection depth, w_b is the rise speed of the bubbles, and h is the water depth.

The diffusion of bubbles as a function of time and depth is illustrated in Figure 5.3a for bubbles with $a = 150 \mu\text{m}$. The distribution spreads with time, and the peak in the distribution will reach the surface in the same time as the still water rise time of a single bubble. Half the bubbles remain suspended when the peak surfaces, so, if the distribution is very spread out, the remaining bubbles will stay in suspension longer than for the case of a narrow distribution.

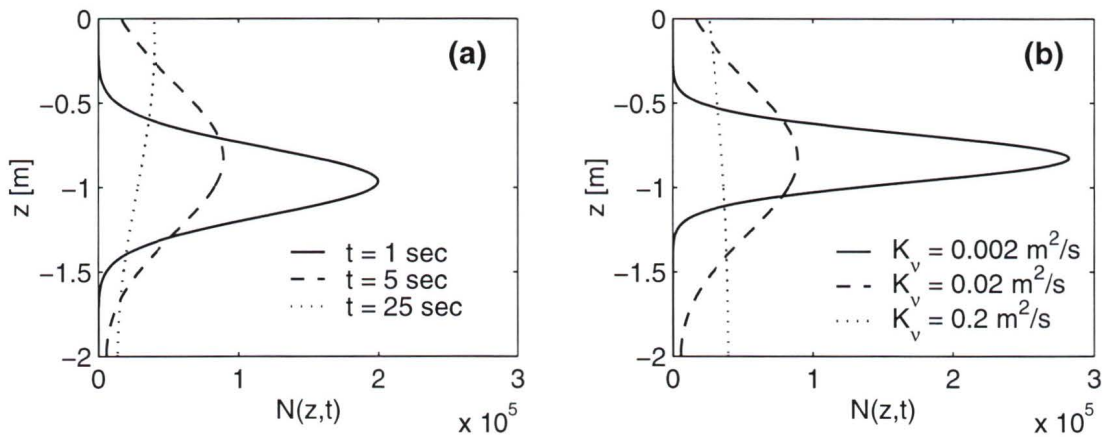


Figure 5.3: *The diffusion of bubbles within a cloud. (a) Time evolution for bubbles of radius $a = 150 \mu\text{m}$ and $K_\nu = 0.02\text{m}^2/\text{s}$. (b) Distribution after $t = 5$ seconds for different values of the diffusion coefficient, K_ν .*

According to this simple model, the spread in the distribution is dependent only on the level of turbulence. Figure 5.3b illustrates the spread in the distribution after 5 seconds for three different values of the diffusion coefficient, corresponding to the extreme and mean values of the eddy viscosity that were derived from the turbulence measurements in the surf zone. The bubbles very quickly become evenly distributed throughout the water column in high turbulence levels.

The spread of the bubble cloud is important when discussing persistent bubble barriers. Unless a large portion of the water column is filled with bubbles, a true barrier will not exist. For the Gaussian solution, the standard deviation is given by $\sigma = \sqrt{2K_v t}$, and a cloud with a full width of 2σ will contain approximately 68% of the bubbles initially injected. Ignoring for the moment the bottom boundary, the width as a function of time is illustrated in Figure 5.4.

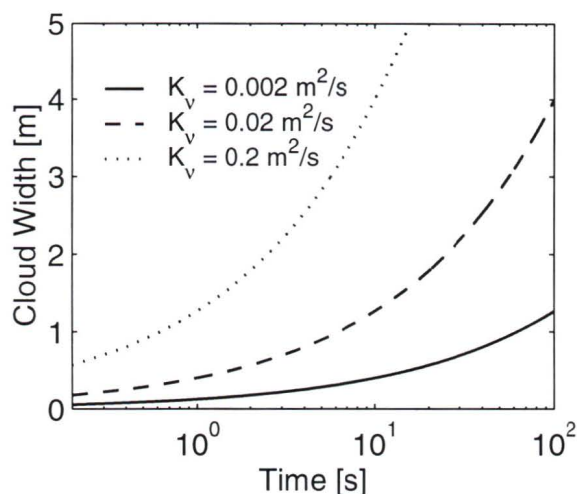


Figure 5.4: *The cloud width as a function of time.*

Before proceeding to a discussion of bubble cloud lifetimes, a discussion of dissolution times is necessary. Using model calculations provided by Svein Vagle [*personal communication*, IOS, 2000], simple estimates for the time a bubble takes to dissolve were obtained, where dissolution in this model is said to occur when the bubble radius is zero. When isolated from pressure effects by forcing the bubble to remain at a depth of 1 m, dissolution is dependent on the gas saturation of the water and the bubble size, as illustrated in Figure 5.5. At saturation levels greater than approximately 110%, bubbles grow in size. Dissolved oxygen measurements obtained at the end of the pier during the 1999 experiment found saturation levels close to 105%. The same will be assumed for the 1997 experiment, when no dissolved oxygen measurements were made.

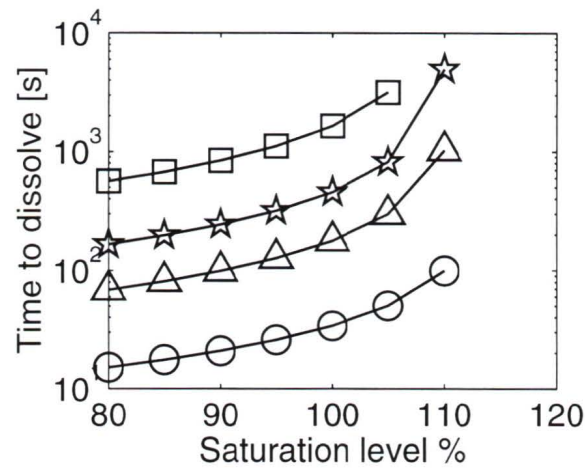


Figure 5.5: *Dissolution time as a function of water saturation level. The bubbles were forced to remain at a depth of 1 m to eliminate pressure effects. Symbols represent bubble radius: 20 μm (\circ); 50 μm (Δ); 100 μm (\star); 300 μm (\square).*

Various time lines as a function of bubble radius are summarized in Figure 5.6. The solid line is the still water rise time, corresponding also to the time it takes for the center of the bubble cloud (of uniformly sized bubbles) to rise to the surface. Except for very small bubbles, this time is always less than the dissolution time of a bubble of the same size. The shaded regions denote, for different turbulence levels, the bubble sizes for which a cloud will still contain at least half the initial number of bubbles when the cloud width is half the water depth. The bottom boundary therefore represents the time required for the cloud width to grow to half the water depth. The life time of the bubble cloud is limited by bubble dissolution at smaller radii, and surfacing of half the bubbles at larger radii.

5.2.4 The Bubble Barrier

A bubble barrier occurs when a bubble cloud persists for an extended period of time. Predicting when a bubble barrier can be created requires a knowledge of the lifetimes of the bubbles in the water and the frequency at which bubbles are renewed through

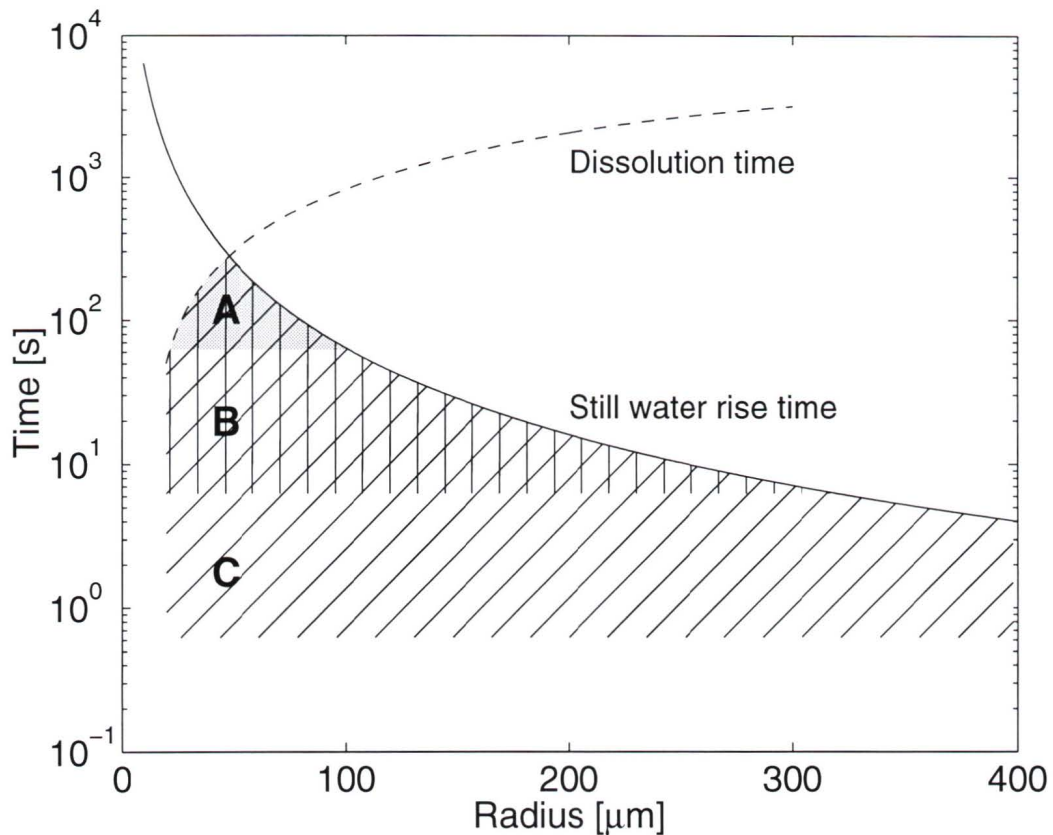


Figure 5.6: Time lines of the various processes as a function of bubble radius. The still water rise time is equivalent to the time required for the peak in the distribution to reach the surface. The dissolution time is for 105% water saturation. The shaded regions denote times when at least half the bubbles at the indicated radii exist as clouds spanning half the water depth or more. Turbulence levels are as follows: A (shading): $K_v = 0.002 \text{ m}^2/\text{s}$; B (vertical hatching): $K_v = 0.02 \text{ m}^2/\text{s}$; C (diagonal hatching): $K_v = 0.2 \text{ m}^2/\text{s}$.

wave breaking. From Figure 5.6, bubbles of sizes detected by the resonator have lifetimes ranging from 4 – 300 seconds. Once the frequency of injection events has been established, the occurrence of bubble barriers can then be discussed.

The intermittency of injection events is determined directly from the frequency at which waves break. Casual observation of the video taken from the pier reveals that the frequency of breaking at any one location depends on the phase of the tide. Waves tend to arrive in packets, with the first and last few waves being smaller than the central ones. As the water depth decreases, the number of breaking waves within the packet increases, with the central waves being the first to break. Three 15 minute segments on 8 March 1997 were examined and the results are summarized in Table 5.1. The third column lists the number of adjacent breaking waves within a packet, and the final column lists the average time interval between successive breaking groups. During low tide, this corresponds to the wave period, which for the experiment ranged from approximately 5 to 10 seconds. At other times, the interval between successive breaking groups ranged from 1 – 10 minutes, since in deeper water, the interval between breaking events was observed to be as great as 10 – 15 minutes.

Start time of 15 minute interval	h	Number of adjacent breaking waves	Time between breaking groups
08:45	2.7 m	1-3	1-2 minutes
09:45	2.4 m	1-7	~ 30 seconds
10:45	2.0 m	~ all	the wave period

Table 5.1: *Summary of the number and frequency of breaking waves at various water depths on 8 March 1997.*

At low tide, every wave breaks. For a wave period of 10 seconds and mean levels of turbulence, a persistent bubble cloud with a wide spectrum of bubble sizes will exist because according to Figure 5.6, bubbles with a radius less than $250\ \mu\text{m}$ will not have reached the surface, nor will they have dissolved completely. Not even the

smallest bubbles measured by the resonator will have dissolved.

As the water depth increases, bubble replenishment occurs less frequently. The size spectrum of the bubble barrier is expected to become more narrow between each of the injection events. When the breaking waves occur at intervals of approximately 30 seconds, bubbles with radii less than $150\ \mu\text{m}$ are expected to persist. When the injection events occur at intervals of 1 minute, only bubbles of radii less than $100\ \mu\text{m}$ will persist, except for the smallest bubbles which have time to dissolve completely between successive breaking waves. The number of smallest bubbles will not be zero, however, since the larger bubbles are also in the process of dissolving. No bubble wall will persist from one injection to the next if the time interval is greater than 5 minutes. All the larger bubbles will surface, and the smaller ones will have time to dissolve completely.

At lower levels of turbulence, the bubbles take longer to diffuse throughout the water column. However, in nature, bubbles are injected at all depths above the maximum injection depth, and a bubble wall may yet be created.

The lifetime of a bubble barrier at any one location is also dependent on background currents. The lifetime may be extended if waves are breaking inshore of the barrier, and these new clouds are carried out by a rip current to replace the older, decaying clouds. Conversely, the lifetime may be shortened if there is either an onshore current or a longshore current.

The bubble barrier can frequently be observed in the 100 kHz Doppler sonar data. The sonar was located at the end of the pier, with measurements being recorded along the shoreward path (Figure 3.1). A short segment is illustrated in Figure 5.7. The bubble clouds are regions of high acoustical backscatter. When the cloud is dense enough, the signal cannot penetrate beyond, and the areas shoreward of the clouds are therefore 'shadow' regions. Because the water depth steadily decreases, continuous breaking occurs, but only the cloud nearest to the sonar is observed.

The cloud located at approximately $150\ \text{m}$ persisted for at least four minutes,

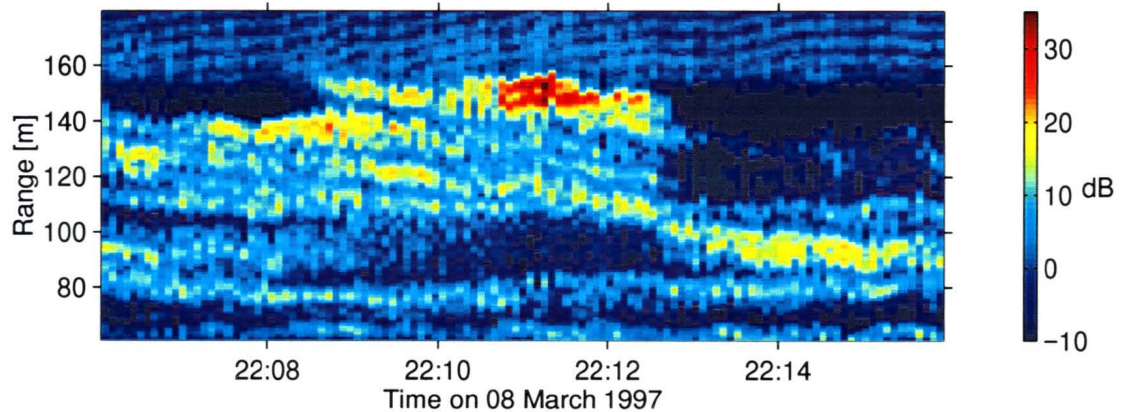


Figure 5.7: Backscatter from beam 2 of the 100 kHz sonar. The dark bands are bubble clouds. The range is distance from the seaward end of the pier.

from 22:09 to 22:13. Beyond 22:13, the cloud has either been advected out of the detection range of the sonar by longshore currents, or it has simply been blocked by an intervening injection event. The cloud must have been regenerated by breaking waves during this time interval. Bubbles with a radius of $35\ \mu\text{m}$, which have a resonant frequency of 100 kHz, would not otherwise survive, since they have a dissolution time of approximately 100 seconds.

The previous discussion will also be used to re-examine the data segment in Figures 4.13 and 4.14. Two bubble sizes in particular will be discussed: $35\ \mu\text{m}$ because it has a resonant frequency of 100 kHz, and $100\ \mu\text{m}$ because it is the radius at which the peak falls in the initial size distribution in Figure 4.14.

Figure 5.8 illustrates the decay in the number of bubbles at these radii during the same time period as in Figure 4.13. The mean water depth is approximately 2 m, so that bubbles measured by the resonator must rise 0.45 m to reach the surface. The lifetime of the bubbles with a $100\ \mu\text{m}$ radius is determined by the rise time, which in this case is approximately 30 seconds. In contrast, the $35\ \mu\text{m}$ bubble lifetimes will be dominated by dissolution, which in 105% saturated water, is approximately 100 seconds. From 0 to 20 seconds in Figure 5.8b, the resonator was saturated. For the

next 60 seconds, the air fraction in Figure 5.8a decays only slightly. The number of bubbles remains essentially constant. At approximately 60 seconds, there is a sharp decay in the number of $100\ \mu\text{m}$ bubbles and the air fraction. The steady decline indicates that there were no injection events during this time. The number of smaller bubbles does not drop so dramatically because their numbers are being replenished by the larger bubbles that dissolve into smaller ones. Even after 60 seconds without replenishment, the number of $100\ \mu\text{m}$ bubbles is still not negligible. Bubbles of size equal to or greater than $100\ \mu\text{m}$ should have risen to the surface in 30 seconds or less, yet a fraction of them remain long after this, illustrating the turbulent suspension of bubbles. This cloud of bubbles would have blocked the 100 kHz sonar for the entire time segment, if no clouds had formed in the intervening region.

5.3 A Final Look at Turbulence in the Surf Zone

The slopes of the velocity spectra calculated from data collected during nearshore field experiments frequently deviate from the $-5/3$ inertial subrange theory. As discussed below, this difference has yet to be satisfactorily explained since, although some suggestions are offered in the literature, they are supported neither by discussion nor by data. What follows is not an attempt to explain this difference, but rather to illustrate what is observed when simultaneous bubble and turbulence measurements are made.

From measurements obtained by a hot film anemometer in the lower portion of the water column within the surf zone, *George et al.* [1994] found the slopes were generally less steep than $-5/3$. They suggested bubbles may in some way be responsible for this, but lacking bubble measurements, were unable to provide support to this statement.

Melville et al. [1997] obtained turbulence measurements in the nearshore region near Scripps Pier with a coherent Doppler. Outside the surf zone, a $-5/3$ slope was found for both longshore and vertical velocities. (For the longshore velocities, the

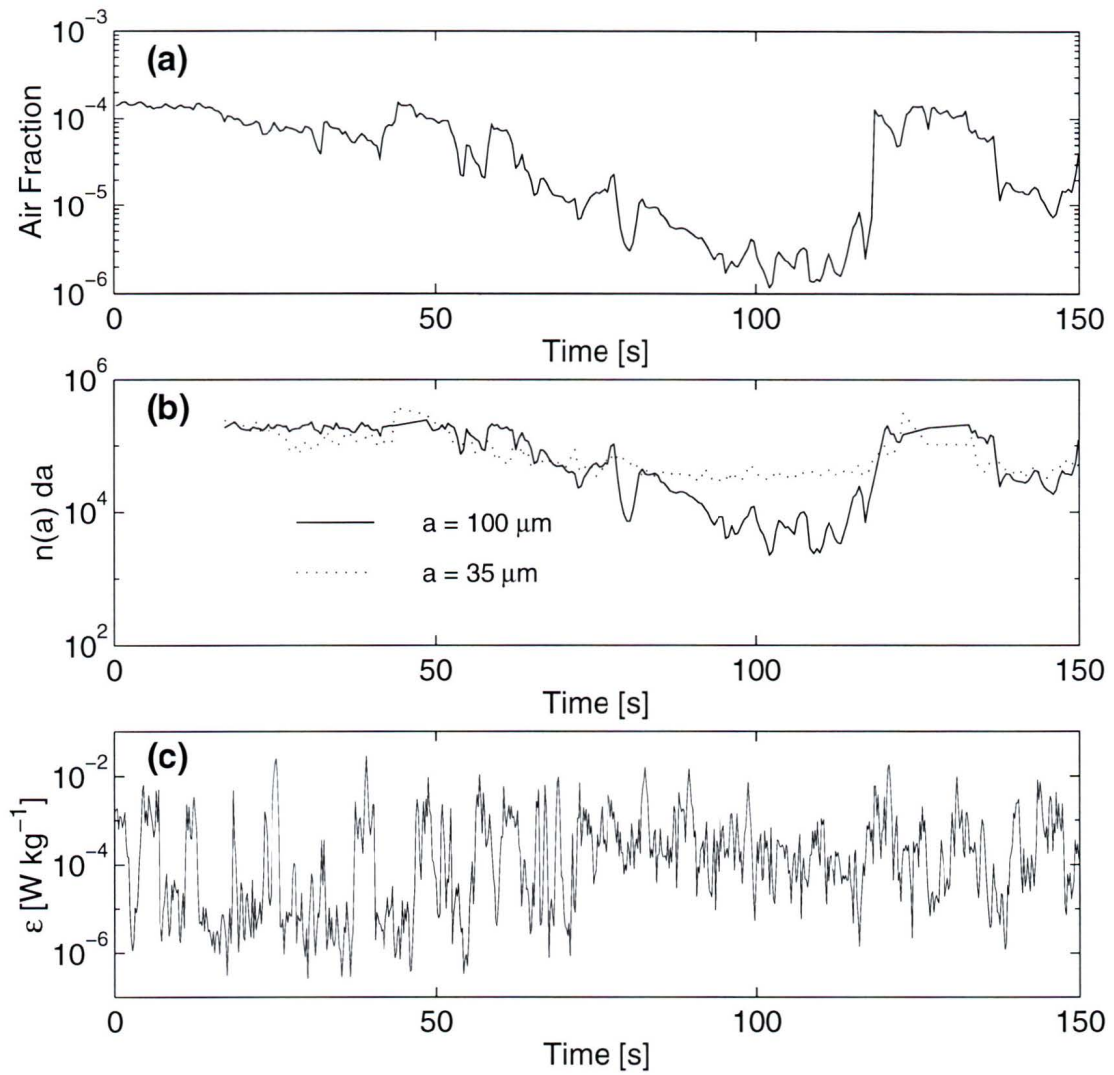


Figure 5.8: (a) Air fraction. (b) Number of bubbles per unit radius of the indicated size. Start time: 5 March 1997 20:04.

$-5/3$ slope was found in the range $6 - 30$ cm; compare this to the region over which I computed the spectrum, $5 - 25$ cm.) Within the surf zone, the slope was again significantly different from the theoretical $-5/3$ slope. In contrast to *George et al.* [1994], they found a steeper slope, and explained this difference without reference to bubbles, suggesting instead that the intermittent generation of turbulence in the surf zone prevented an inertial subrange from being maintained.

Returning to the histograms in Figure 4.8, it is seen that the spectral slopes obtained during the 1997 experiment are centered about the theoretical $-5/3$ in deep water when the number of breakers is low. Like *Melville et al.* [1997], the slopes tend to steepen within the surf zone. This seems to be in contradiction with the results of *George et al.* [1994], although perhaps the difference in instrumentation and sampling depth may account for the discrepancy.

The data collected in 1997 are unique in that simultaneous measurements of turbulence and bubbles were obtained. Comparisons of air fraction with velocity spectral slopes will be made in an attempt to understand if it is the bubbles that are affecting the turbulence. The air fraction has been plotted against the spectral slope in Figure 5.9. Only three segments where a small time lag between the instruments could be corrected with confidence were used in the plot. This included one at high tide (low air fraction) and two at low tide (high air fraction), hence the gap at air fractions near 10^{-8} . If bubbles were causing the slopes to deviate from theory, we would expect the slope to be near $-5/3$ at low air fraction and far from $-5/3$ at high air fraction. A very slight trend does exist, although even at low air fractions, the slopes are still less than $-5/3$. This is not sufficient to state that bubbles have a significant direct effect on the turbulence.

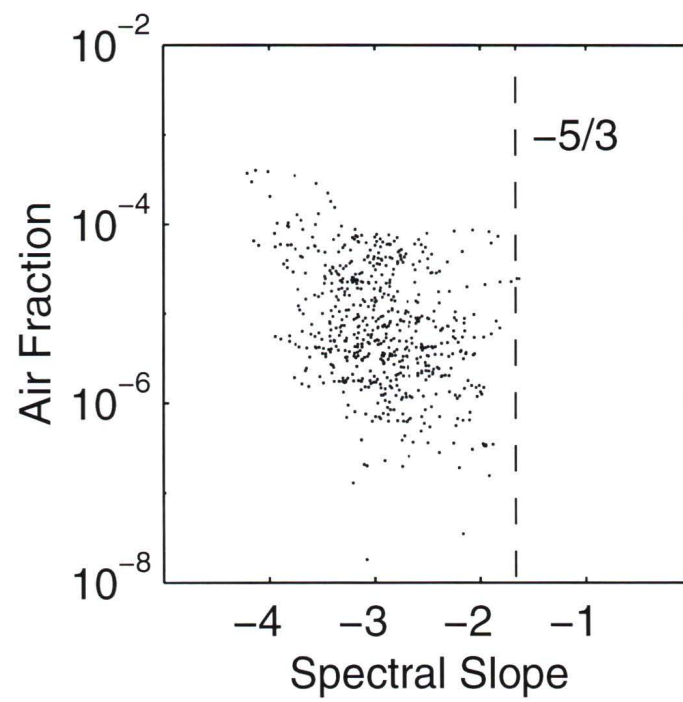


Figure 5.9: Scatter plot of the air fraction against the velocity spectral slope.

6 Summary

6.1 Summary

This thesis examines the energetics of the nearshore region and the interactions between turbulence and bubbles. It fills a gap in experimental studies as it is the first of its kind, in the natural setting or the laboratory, to collect simultaneous measurements of turbulence and bubbles. The measurements were collected during a collaborative experiment in the surf zone near Scripps Pier in 1997 that was designed to study the effects of bubbles on high frequency acoustic propagation. Because many different investigators participated, a comprehensive set of results and references exist (see, for example, *Vagle et al.* [in press, 2000]), from which a broader understanding of this particular environment can be gained.

The measurements of primary interest to this study were the surface elevation, turbulent velocities, and bubble size distributions. With the water level oscillating as the tide moved in and out, measurements were obtained by the fixed instrument in various regions of the surf zone. Thus, in addition to a time series being obtained, on a longer time scale, measurements were collected as a function of distance from the main breaker line and as a function of depth beneath the mean surface.

Potential and kinetic energy was estimated from the surface wave profile by applying linear wave theory to the Fourier decomposition of the time series. Linear theory

was found to provide excellent results even within the surf zone since the evolution of the nonlinear surface boundary was already known. The wave energy dissipation rate was then computed from the gradient of the energy flux.

The wave energy dissipation rate was found to be at least an order of magnitude greater than the dissipation rate measured by the coherent Doppler within the water column. Simple calculations were therefore performed to estimate the magnitude of other possible energy sinks within the surf zone. At an order of magnitude less than the wave energy dissipation, neither the energy required to force bubbles into the water to the depth of the instrument, nor the energy loss to friction at the sea floor could account for the large wave energy dissipation. It would therefore appear that much of the energy is dissipated by turbulence in the region above the instruments where the turbulence rapidly decays, with only a small fraction diffusing into the interior of the water column. Some of the wave energy may also be dissipated during the entrainment of air in the high air fraction region above the wave trough. Also of significance is the low bottom boundary dissipation rate. Since the sea floor does not seem to play a dominant role in turbulence production, results from surf zone experiments can be translated to the open ocean with greater confidence.

The role intermittency, bubble buoyancy, dissolution, and turbulence play in the generation of persistent bubble clouds was examined. A simple model for the diffusion of bubbles was used to determine the time required for a bubble wall to be generated.

The effect bubbles may have on the turbulence was also explored, although no direct effect was observed. Some investigators suggested bubbles may be the reason spectral slopes frequently deviate from theory, but no obvious relation between air fraction and slope was observed.

6.2 Recommendations for Future Work

This work is the first step towards observing the relationship between turbulence and bubbles in the natural surf zone. Much more could be gained by looking at the turbulence immediately following an isolated breaking event. To positively identify breaking waves, video recordings throughout the entire measurement period would be invaluable. Of particular interest is the rate of decay of turbulence and the depth dependence. A one-to-one comparison between bubble measurements and turbulence data was hindered by a drifting time lag between the two instruments. This lag could only be accounted for with confidence when the coherent Doppler was in a cross-shore orientation and could therefore measure the wave orbital velocity. Overcoming this problem requires either a solution to the time lag or positioning the coherent Doppler in a cross-shore orientation, although *He* [1997] recommended the long-shore orientation in order to minimize the effect of the wave motion in the turbulent calculations.

Despite the spatial measurements that were provided by fixed instruments in the changing tide, an array of instruments would provide additional insight into the distribution with depth. This was attempted in 1999 when three frames, supporting five resonators and three coherent Doppler sonars, was positioned in the same location as the earlier experiment. Unfortunately, there was an unforeseen problem with the sonar (the cable was violently ripped off the instrument during the first low tide!) It would be interesting to perform this experiment again, particularly in the same location so that insights and results from the previous experiments could be applied.

The interactions between turbulence and bubbles should be revisited with longer segments of turbulence data to determine with greater certainty whether bubbles have a significant effect on the nature of turbulence within the surf zone. A controlled laboratory study of this problem might be useful. Finally, a bubble model incorporating the interdependent processes is required, and is the topic of ongoing research.

Bibliography

- Battjes, J. A., Surf similarity, in *Proceedings of the 14th Coastal Engineering Conference*, pp. 466–480, New York, NY, 1974.
- Battjes, J. A., Surf-zone dynamics, *Annual Review of Fluid Mechanics*, 20, 257–293, 1988.
- Cabrera, R., K. Deines, B. Brumley, and E. Terray, Development of a practical coherent acoustic doppler current profiler, in *Proc. Oceans '87*, pp. 93–97, 1987.
- Christoffersen, J. B., and I. G. Jonsson, Bed friction and dissipation in a combined current and wave motion, *Ocean Engineering*, 12, 387–423, 1985.
- Dean, R. G., and R. A. Dalrymple, *Water Wave Mechanics for Engineers and Scientists*, World Scientific Publishing Co. Pte. Ltd., London, 1991.
- Deane, G. B., Sound generation and air entrainment by breaking waves in the surf zone, *Journal of the Acoustical Society of America*, 102, 2674–2689, 1997.
- Deane, G. B., and M. D. Stokes, Air entrainment processes and bubble size distributions in the surf zone, *Journal of Physical Oceanography*, 29, 1393–1403, 1999.
- Farmer, D. M., C. L. McNeil, and B. D. Johnson, Evidence for the importance of bubbles in increasing air-sea gas flux, *Nature*, 361, 620–623, 1993.
- Farmer, D. M., S. Vagle, and A. D. Booth, A free-flooding acoustical resonator for measurement of bubble size distributions, *Journal of Atmospheric and Oceanic Technology*, 15, 1132–1146, 1998.
- Farmer, D. M., G. B. Deane, and S. Vagle, The influence of bubble clouds on acoustic propagation in the surf zone, *IEEE Ocean Engineering*, 2000, accepted.
- Fischer, H. B., E. J. List, R. C. Y. Koh, J. Imberger, and N. H. Brooks, *Mixing in Inland and Coastal Waters*, Academic Press, New York, 1979.
- Fredsøe, J., and R. Deigaard, *Mechanics of Coastal Sediment Transport*, World Scientific, London, 1992.

- Garrett, C., M. Li, and D. Farmer, The connection between bubble size spectra and energy dissipation rates in the upper ocean, *Journal of Physical Oceanography*, *30*, 2163–2171, 2000.
- George, R., R. E. Flick, and R. T. Guza, Observations of turbulence in the surf zone, *Journal of Geophysical Research*, *99*, 801–810, 1994.
- Grant, W. D., and O. S. Madsen, Combined wave and current interaction with a rough bottom, *Journal of Geophysical Research*, *84*, 1797–1808, 1979.
- He, Y., High frequency coherent doppler sonar for probing surf zone turbulence, Master's thesis, University of Victoria, Victoria, BC, Canada, 1997.
- Hinze, J. O., *Turbulence*, 2nd ed., McGraw-Hill, New York, NY, 1975.
- Inman, D. L., R. J. Tait, and C. E. Nordstrom, Mixing in the surf zone, *Journal of Geophysical Research*, *76*, 3493–3514, 1971.
- Jonsson, I. G., Wave boundary layers and friction factors, in *Proceedings of the 10th Coastal Engineering Conference*, pp. 127–148, American Society of Civil Engineers, New York, NY, 1966.
- Kamphuis, J. W., Wave transformation, *Coastal Engineering*, *15*, 173–184, 1991.
- Keeling, R. F., On the role of large bubbles in air-sea gas exchange and supersaturation in the ocean, *Journal of Marine Research*, *51*, 237–271, 1993.
- Komar, P. D., *Beach Processes and Sedimentation*, 2nd ed., Prentice Hall, New Jersey, 1998.
- Kundu, P. K., *Fluid Mechanics*, Academic Press, San Diego, CA, 1990.
- Lamarre, E., and W. K. Melville, Air entrainment and dissipation in breaking waves, *Nature*, *351*, 469–472, 1991.
- Lamarre, E., and W. K. Melville, Instrumentation for the measurement of void-fraction in breaking waves: Laboratory and field results, *IEEE Journal of Oceanic Engineering*, *17*, 204–215, 1992.
- Leighton, T. G., *The Acoustic Bubble*, Academic Press, 1994.
- Lin, P., and P. L.-F. Liu, A numerical study of breaking waves in the surf zone, *Journal of Fluid Mechanics*, *359*, 239–264, 1998.
- Lumley, J. L., and E. A. Terray, Frequency spectra of frozen turbulence in a random wave field, *Journal of Physical Oceanography*, *13*, 2000–2007, 1983.

- Medwin, H., and N. D. Breitz, Ambient and transient bubble spectral densities in quiescent seas and under spilling breakers, *Journal of Geophysical Research*, *94*, 12,751–12,759, 1989.
- Melville, W. K., E. Terrill, and F. Veron, Bubbles and turbulence under breaking waves, in *Natural Physical Processes Associated with Sea Surface Sound*, edited by T. G. Leighton, pp. 135–145, University of Southampton, 1997.
- Miller, R. L., Role of vortices in surf zone prediction: Sedimentation and wave forces, *Beach and Nearshore Sedimentation, SEPM Spec. Pub.*, *23*, 92–114, 1976.
- Monahan, E. C., Occurrence and evolution of acoustically relevant sub-surface bubble plumes and their associated, remotely monitorable, surface whitecaps, in *Natural Physical Sources of Underwater Sound*, edited by B. R. Kerman, pp. 503–517, Kluwer Academic Publishers, Netherlands, 1993.
- Nadaoka, K., M. Hino, and Y. Koyano, Structure of turbulent flow field under breaking waves in the surf zone, *Journal of Fluid Mechanics*, *204*, 359–387, 1989.
- Nielsen, P., Turbulence effects on the settling of suspended particles, *Journal of Sedimentary Petrology*, *63*, 835–838, 1993.
- Ninnis, R., Theory of void fraction sensors, *Tech. Rep. IOSPB-CR-301*, Insitute of Ocean Sciences, B.C., Canada, 1991.
- Pidgeon, E. J., An experimental investigation of breaking wave induced turbulence, Ph.D. thesis, Stanford University, 1999.
- Richardson, L. F., *Weather Prediction by Numerical Process*, Dover, 1965.
- Sarpkaya, T., and M. Isaacson, *Mechanics of Wave Forces on Offshore Structures*, Van Nostrand Reinhold Company, Toronto, 1981.
- Shemdin, O. H., K. Hasselmann, S. V. Hsiao, and K. Herterich, Nonlinear and linear bottom interaction effects in shallow water, in *Turbulence Fluxes Through the Sea Surface, Wave Dynamics, and Prediction*, edited by A. Favre and K. Hasselmann, pp. 347–372, Plenum Press, New York, 1978.
- Stokes, M. D., and G. B. Deane, A new optical instrument for the study of bubbles at high void fractions within breaking waves, *IEEE Journal of Oceanic Technology*, *24*, 300–311, 1999.
- Svendsen, I. A., Analysis of surf zone turbulence, *Journal of Geophysical Research*, *92*, 5115–5124, 1987.
- Svendsen, I. A., Surf zone dynamics, in *IUTAM Symposium*, edited by M. L. Banner and R. H. J. Grimshaw, pp. 55–68, Sidney, Australia, 1991.

- Tennekes, H., and J. L. Lumley, *A First Course in Turbulence*, The MIT Press, Cambridge, MA, 1972.
- Terrill, E. J., Acoustic measurements of air entrainment by breaking waves, Ph.D. thesis, University of California, San Diego, 1998.
- Terrill, E. J., and W. K. Melville, A broadband acoustic technique for measuring bubble size distributions: Laboratory and shallow water measurements, *Journal of Atmospheric and Oceanic Technology*, *17*, 220–239, 2000.
- Thornton, E. B., Energetics of breaking waves within the surf zone, *Journal of Geophysical Research*, *84*, 4931–4938, 1979.
- Thorpe, S. A., On the clouds of bubbles formed by breaking wind-waves in deep water, and their role in air-sea gas transfer, *Philosophical Transactions of the Royal Society of London A*, *304*, 155–210, 1982.
- Thorpe, S. A., A model of the turbulent diffusion of bubbles below the sea surface, *Journal of Physical Oceanography*, *14*, 841–854, 1984a.
- Thorpe, S. A., On the determination of k_v in the near-surface ocean from acoustic measurements of bubbles, *Journal of Physical Oceanography*, *14*, 855–863, 1984b.
- Ting, F. C. K., and J. T. Kirby, Dynamics of surf-zone turbulence in a spilling breaker, *Coastal Engineering*, *27*, 131–160, 1996.
- Vagle, S., and D. M. Farmer, A comparison of four methods for bubble size and void fraction measurements, *IEEE Journal of Oceanic Technology*, *23*, 211–222, 1998.
- Vagle, S., D. M. Farmer, and G. B. Deane, Bubble transport in rip currents, *Journal of Geophysical Research*, in press, 2000.
- Wang, H., D.-Y. Lee, and A. Garcia, Time series surface-wave recovery from pressure gage, *Coastal Engineering*, *10*, 379–393, 1986.
- Zedel, L., and A. E. Hay, A coherent doppler profiler for high-resolution particle velocimetry in the ocean: Laboratory measurements of turbulence and particle flux, *Journal of Atmospheric and Oceanic Technology*, *16*, 1102–1117, 1999.
- Zedel, L., A. E. Hay, R. Cabrera, and A. Lohrmann, Performance of a single-beam pluse-to-pulse coherent doppler profiler, *IEEE Journal of Oceanic Engineering*, *21*, 290–297, 1996.

VITA

Surname: Kendall

Given Names: Roblyn

Place of Birth: Scarborough, Ontario, Canada

Educational Institutions Attended:

University of Toronto	1994 to 1998
University of Victoria	1998 to 2001

Degrees Awarded:

B.Sc. (Honours) University of Toronto	1998
---------------------------------------	------

Honours and Awards:

KEGS - Award in Geophysics	1997 to 1998
Victoria College Chancellor's Scholarship (UofT)	1997

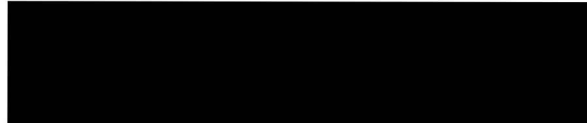
PARTIAL COPYRIGHT LICENSE

I hereby grant the right to lend my thesis to users of the University of Victoria Library, and to make single copies only for such users or in response to a request from the Library of any other university, or similar institution, on its behalf or for one of its users. I further agree that permission for extensive copying of this thesis for scholarly purposes may be granted by me or a member of the University designated by me. It is understood that copying or publication of this thesis for financial gain shall not be allowed without my written permission.

Title of Thesis:

**An Investigation into the Energetics of the Surf Zone
and the Interactions between Turbulence and Bubbles**

Author:



Roblyn Kendall
March 29, 2001